Listeria monocytogenes InlP interacts with afadin and facilitates basement membrane crossing

Cristina Faralla[a,b,i] *, Effie E. Bastounis[c] *, Fabian E. Ortega[c] , Samuel H. Light[d], Gabrielle Rizzuto[a,b] , Salvatore Nocadello[d], Wayne F. Anderson[d], Jennifer R. Robbins[e], Julie A. Theriot[c,f,g], and Anna I. Bakardjiev[a,b,h]

*These authors contributed equally

[a] Benioff Children's Hospital, University of California, San Francisco, San Francisco, California;

[b]Program in Microbial Pathogenesis and Host Defense, University of California, San Francisco, San Francisco, California;

[c]Department of Biochemistry, Stanford University School of Medicine, Stanford, California;

[d]Center for Structural Genomics of Infectious Diseases and Department of Biochemistry and Molecular Genetics, Feinberg School of Medicine, Northwestern University, Chicago, Illinois;

[e]Department of Biology, Xavier University, Cincinnati, Ohio;

[f]Department of Microbiology and Immunology, Stanford University School of Medicine, Stanford, California;

[g]Howard Hughes Medical Institute, Stanford University School of Medicine, Stanford, California;

[h]Current address: VIR Biotechnology, San Francisco, California

[i]Current address: AbCellera Biologics Inc., Vancouver, BC, Canada

Corresponding author: abakardjiev@vir.bio

Short title: *L. monocytogenes* InlP binds afadin

ABSTRACT

During pregnancy, the placenta protects the fetus against the maternal immune response, as well as bacterial and viral pathogens. Bacterial pathogens that have evolved specific mechanisms of breaching this barrier, such as *Listeria monocytogenes*, present a unique opportunity for learning how the placenta carries out its protective function. We previously identified the *L. monocytogenes* protein Internalin P (InlP) as a secreted virulence factor critical for placental infection (1). Here, we show that InlP, but not the highly similar *L. monocytogenes* internalin Lmo2027, binds to human afadin (encoded by *AF-6*), a protein associated with cell-cell junctions. A crystal structure of InlP reveals several unique features, including an extended leucine-rich repeat (LRR) domain with a distinctive Ca^{2+}-binding site. Despite afadin's involvement in the formation of cell-cell junctions, MDCK epithelial cells expressing InlP displayed a decrease in the magnitude of the traction stresses they could exert on deformable substrates, similar to the decrease in traction exhibited by *AF-6* knock-out MDCK cells. *L. monocytogenes ΔinlP* mutants were deficient in their ability to form actin-rich protrusions from the basal face of polarized epithelial monolayers, a necessary step in the crossing of such monolayers (transcytosis). A similar phenotype was observed for bacteria expressing an internal in-frame deletion in *inlP* (*inlP* ΔLRR5) that specifically disrupts its interaction with afadin. However, afadin deletion in the host cells did not rescue the transcytosis defect. We conclude that secreted InlP targets cytosolic afadin to specifically promote *L. monocytogenes* transcytosis across the basal face of epithelial monolayers, which may contribute to the crossing of the basement membrane during placental infection.

46 **INTRODUCTION**

47 During pregnancy, the consequences of placental infection can be severe, ranging from
48 maternal sepsis to miscarriage, and can lead to pre-term birth and lifelong disability (2).
49 Fortunately, such infections are relatively rare – which stands as a testament to the strength of the
50 feto-maternal barrier. Despite serving such an important function, the molecular, cellular and
51 histological components of feto-maternal barrier have only just begun to be elucidated. Because
52 the barrier is so effective at preventing infection, pathogens that do manage to cross it must have
53 evolved strategies of countering host defenses and thus provide a unique opportunity for
54 addressing the mechanistic features that make the feto-maternal barrier so formidable (3).

55 *Listeria monocytogenes* is a well-characterized food-borne pathogen capable of
56 placental crossing and is thus ideal for probing the barrier (4). In the healthy, non-pregnant adult,
57 it causes gastrointestinal illness, but in immunocompromised individuals meningitis can result,
58 and in pregnant women, sepsis, spontaneous abortion, preterm labor, infant brain damage and
59 death are possible outcomes (5). After ingestion, *L. monocytogenes* infects epithelial cells of the
60 intestine, mainly via interactions between the bacterial surface protein Internalin (encoded by the
61 gene *inlA*) and the host cell receptor E-cadherin, which is exposed at the tips of intestinal villi (6-
62 8). After uptake by an intestinal epithelial cell, the bacterium escapes the resulting phagosome and
63 replicates in the host cytoplasm, where it induces actin polymerization, forming actin comet tails
64 that drive its rapid motility (9). Upon reaching the host plasma membrane, *L. monocytogenes* can
65 form a membrane-bound protrusion that pushes its way into a neighboring cell. Engulfment of the
66 protrusion by the neighboring cell leaves the bacterium in a double-membrane vacuole from
67 which it escapes, resetting its life cycle (9, 10). From the initial site of infection in the intestinal
68 epithelium, *L. monocytogenes* can spread via actin-based motility into immune cells, which

69 facilitate spread throughout the host while protecting the pathogen from humoral immune
70 defenses (11, 12). Actin-based cell-to-cell spread is thought to contribute to the ability of *L.*
71 *monocytogenes* to evade the host immune system and to penetrate a variety of protective barriers
72 in the host (13), including the blood-brain barrier and the feto-maternal barrier in the placenta (14-
73 16).

74 A clue to the protective nature of the feto-maternal barrier lies in the fact that almost all
75 pathogens that cross it are known to have an intracellular aspect to their life cycle—they move
76 *through* cells from mother to fetus (3). Two interfaces are available; each is unlike any other part
77 of the mammalian body. The first, where fetal extravillous trophoblasts (EVTs) anchor the
78 placenta in uterine decidua, has a unique immune environment (17). The trophoblasts possess
79 innate immune defense properties shown to prevent bacterial infection (18) and restrict growth of
80 intracellular *L. monocytogenes* (19). The second, much more extensive interface is composed of
81 fetal syncytiotrophoblasts (STB) which form a vast, thin multinucleate layer without cell-cell
82 junctions, bathed in maternal blood. This is the site of gas and nutrient/waste exchange.
83 Underlying the STB is a second, single-celled layer of individual, self-renewing cytotrophoblasts
84 (CTBs) that periodically fuse with the STB to allow its growth. Our previous work has shown that
85 the STB's lack of cell-cell junctions (20) and the syncytial stiffness generated by dense networks
86 of actin filaments (21) act as significant deterrents to STB infection by pathogens. Rather,
87 infection of human placental organ cultures suggests that the first interface, where EVTs contact
88 uterine decidua, is the preferred route of placental infection by *L. monocytogenes*, which then
89 spreads via actin-dependent cell-to-cell spread to the CTB monolayer underlying the STB (20).
90 But even once *L. monocytogenes* has reached the subsyncytial CTBs, most bacterial movement

91 occurs laterally from cell to cell within the monolayer, and it only rarely transcytoses in a
92 direction perpendicular to the monolayer to colonize the fetal stroma beneath it (20).
93 Recently, we used an unbiased genetic screen in a pregnant guinea pig model of listeriosis
94 to identify *L. monocytogenes* genes that contribute specifically to infection of the placenta. (1).
95 One gene identified in this screen encodes InlP, a member of the internalin family of proteins.
96 Pathogenic *L. monocytogenes* contain genes for 25 known members of this protein family, which
97 share a common overall structure that includes a secretory signal sequence at the N terminus and a
98 large leucine-rich repeat domain, a motif frequently implicated in protein-protein interactions
99 (22). The two best-characterized internalins, InlA and InlB, contribute to *L. monocytogenes*
100 invasion of epithelial cells and hepatocytes by binding to their cognate host cell surface receptors,
101 E-cadherin and c-Met respectively (6, 23). While most internalins are predicted to be anchored to
102 the bacterial cell surface via attachment to the peptidoglycan cell wall or to lipoteichoic acids,
103 four of them, including InlP, lack obvious anchoring domains and are predicted to be secreted by
104 the bacterium (24). In order to address the mechanism by which InlP assists *L. monocytogenes* in
105 crossing the feto-maternal barrier, we set out to find host protein binding partners. In this work,
106 we identify the host cell cytoplasmic protein afadin as a major binding partner for InlP, and
107 demonstrate that the InlP-afadin interaction specifically enhances *L. monocytogenes*
108 transcytosis—that is, the ability of *L. monocytogenes* to exit from the basal face of an infected
109 polarized epithelial monolayer, consistent with its potential contribution to placental infection.

110 **MATERIALS AND METHODS**

111 **Study approval.** Human subjects: This study was conducted according to the principles
112 expressed in the Declaration of Helsinki. The study was approved by the Institutional Review
113 Board at the University of California, San Francisco, where all experiments were performed
114 (CHR# 11-05530). All patients provided written informed consent for the collection of samples
115 and subsequent analysis.

116 **Recombinant InlP expression and purification.** All chemicals were purchased from
117 Sigma-Aldrich unless otherwise stated. Center for the Structural Genomics of Infectious Diseases
118 (CSGID) standard protocols were used for cloning, over-expression, and purification of InlP (25,
119 26). Briefly, InlP (from residue 31-388) and Lmo2027 (from residue 31-367) were cloned into the
120 pMCSG7 expression vector (http://bioinformatics.anl.gov/mcsg/technologies/vectors.html).
121 Following transformation into the BL21 (DE3) Magic *E. coli* strain, cells were grown in
122 M9-selenomethionine medium or Terrific Broth (TB) at 37 °C up to an OD_{600} of 1. At that point,
123 the temperature was reduced to 25 °C and protein over-expression was induced by the addition of
124 isopropyl-1-thio-D-galactopyranoside (IPTG) to a final concentration of 1 mM. After 16 h, cells
125 were harvested by centrifugation, suspended in a buffer containing 10 mM Tris-HCl pH 8.3, 500
126 mM NaCl, 10% glycerol, and 1 mM Tris (2-carboxyethyl) phosphine hydrochloride (TCEP) and
127 lysed by sonication. InlP was purified by Ni-NTA affinity chromatography and eluted with a
128 buffer containing 10 mM Tris-HCl pH 8.3, 500 mM NaCl, 1 mM TCEP. The His-tag was cleaved
129 overnight at 4°C incubating the enzymes with His-tagged TEV protease. The protein samples
130 were then reloaded onto the nickel column and the flow-through was collected. At this point, the
131 protein was concentrated using Vivaspin centrifugal concentrators (GE Healthcare Life Sciences)

132 and both its size and purity were checked by SDS-PAGE.

133

134 **InlP and Lmo2027 structure determination.** Sitting drop crystallization plates were set
135 up at room temperature. InlP crystals were obtained with a 1:1 mixture of 8.5 mg/mL InlP in 10
136 mM Tris pH 8.3, 1 mM TCEP and condition D11 from the Qiagen PACT crystallization screen
137 (0.2 M Calcium chloride, 0.1 M Tris pH 8, 20% (w/v) PEG 6000). Lmo2027 crystals were
138 obtained with a 1:1 mixture of 12.6 mg/mL Lmo2027 and 10 mM Tris pH 8.3, 0.5 M NaCl, and 1
139 mM TCEP and condition D4 from the Qiagen Classics II crystallization screen (0.1 M Citric acid
140 (pH 3.5) and 20% (w/v) PEG 3350). Harvested crystals were transferred to the mother liquor
141 before being frozen in liquid nitrogen. Diffraction data were collected at 100° K at the Life
142 Sciences Collaborative Access Team at the Advance Photon Source, Argonne, Illinois (APS
143 BEAMLINE 21-ID-G). All structural work was performed by the CSGID (25). Data were
144 processed using HKL-2000 for indexing, integration, and scaling (27). A selenomethionine
145 derivative of InlP was used to phase the structure by single-wavelength anomalous diffraction.
146 Lmo2027 was phased by molecular replacement, using the InlP structure as a starting model.
147 Structure was refined with Refmac (28). Models were displayed in Coot and manually corrected
148 based on electron density maps (29). All structure figures were prepared using PyMOL Molecular
149 Graphics System, Version 1.3 (Schrödinger, LLC).

150

151 **Isothermal titration calorimetry (ITC).** For ITC experiments, InlP was prepared by
152 overnight dialysis in ITC buffer (50 mM HEPES pH 7.5 and 150 mM NaCl). Experiments were
153 performed on the MicroCal ITC200 instrument (GE Healthcare). InlP was loaded into the cell at
154 0.12 mM and 25° C. Calcium chloride titrant (3.13 mM) dissolved in leftover dialysis buffer was

155 loaded into the syringe. Syringe rotation was set at 1000 RPM, with titrant injections spaced at
156 2 min intervals. The initial 0.2 µL injection was excluded from the data and the nineteen
157 subsequent 2.0 µL injections were used for data analysis. Binding parameters were obtained by
158 fitting isotherms using the Origin 7 (OriginLab, Northampton, MA) software package.
159
160 **Yeast two-hybrid, mass spectrometry and pull-down assay.** Yeast two-hybrid analysis
161 was performed by Hybrigenics (France). Briefly, InlP (aa 31-388) was used to screen a human
162 placenta cDNA library. Clones expressing proteins with positive interactions with InlP were
163 isolated and sequenced.
164 For the GST-pull down experiments bait proteins were prepared as follows: Cloning: *inlP*
165 gene (from residue 31-388, oligo Fw2470 EcoRI-pGex CCGAATTCC
166 GCTTCTGATTTATATCCACTACCT, Rv2470 XhoI-pGex aGCTCGAG
167 TCATTAATAGTTACATTCCAATCATAAGAG) or Lmo2027 (from residue 31-367, oligo
168 Fw2027 EcoRI-pGex CCCCGAATTCCGCATCCGATTTATATCCACT ACC, Rv2027 XhoI-
169 pGex GAAGCTCGAGCTACTAATTAACCGTAAGTACCC) were cloned in pGEX-4T vector
170 (GE Healthcare) using restriction enzymes following transformation in BL21 DE3 *E. coli* strain.
171 InlPΔLRR5, InlPΔLRR7 and InlPΔLRR8, lacking the LRR5 (Δamino acids 174-195), the LRR7
172 motifs (Δamino acids 218-239) and the LRR8 (Δamino acids 240-261) respectively were
173 generated using Site Directed Mutagenesis (SDM) on the *inlP*-pGEX-4T vector following In-
174 Fusion® HD Cloning Kit protocol (Takara Bio USA, Inc.) using the following primers : ΔLRR5-
175 fw:GATTTCACTGGAATGCCTATTCCTTTACTTATTACGTTGGATCTAAG, ΔLRR5-rv:
176 CGTAATAAGTAAAGGAATAGG CATTCCAGTGAAATCAGGGATAGA; ΔLRR7-fw
177 CCTGATTTTCAAAATTTACCT AAATTAACTGATTTAAATTTAAGAC, ΔLRR7-rv:

178 AGTTAATTTAGGTAAATTTTGAAAATCAGGAATAGTTGTCA, ΔLRR8-fw:
179 CCTGATTTTCAAA ATAACTTACCTAGTTTAGAATCCTTAAACT ΔLRR8-rv:
180 TAAACTAGGTAAGTTATTTTGAAAATCAGGTGTATTGGTTAA. Baits purification: BL21
181 DE3 *E. coli* carrying pGEX-4T, pGEX-4T-*2027,* pGEX-4T-*inlP,* pGEX-4T-*inlP*Δ*LRR5,* pGEX-
182 4T-*inlP*Δ*LRR7* or pGEX-4T-*inlP*Δ*LRR8,* were grown until OD 0.6 in 250 mL of LB
183 supplemented with 100 µg/mL ampicillin at 37 °C and 180 rpm. GST or GST-
184 InlP/2027/ΔLRR5/ΔLLR7/ΔLRR8 expression were then induced with 0.2 mM IPTG for 4 h at
185 30 °C 180 rpm. Pellet from 250 mL of culture was lysed with 35 mL of cell lytic express (Sigma)
186 and the soluble fraction was incubated overnight with 5 mL of Glutathione Sepharose™ 4B (GE
187 Healthcare) under constant agitation. GST-Glutathione Sepharose™ 4B or GST-
188 InlP/2027/ΔLRR5/ΔLLR7/ΔLRR8/ - Glutathione Sepharose™ 4B were then collected and washed
189 with 100 mL of PBS at 500 x g and stored at 4 °C in Tris-HCl 50 mM, NaCl 50 mM pH 8.
190 For preparation of protein extracts for pull-down experiments with human placenta: 2.3
191 grams of placental villi (~21 weeks gestational age) were lysed in 10 mL of M-PER™ (Thermo
192 Fisher Scientific) supplemented with one tablet of complete Protease Inhibitor Cocktail (Roche)
193 and PhosSTOP phosphatase inhibitor (Roche). The sample was homogenized for 30 sec, sonicated
194 for 4 min and incubated for 1 h on ice. The soluble fraction was collected after centrifugation
195 14000 x g for 20 min at 4 °C, split in two and incubated overnight under constant agitation with 1
196 mL of GST-Glutathione Sepharose™ 4B, GST-InlP- Glutathione Sepharose™ 4B or GST-2027-
197 Glutathione Sepharose™ 4B respectively (prepared previously). The next day, washes were
198 performed with 50 mL PBS and elution fractions were collected with 3 mL Tris-HCl 50 mM,
199 NaCl 50 mM free glutathione 10 mM, pH 8. Elution fractions were run on 10% gel (NuPAGE™
200 Novex™ 10% Bis-Tris Protein Gels) and analyzed by Western blot, Coomassie blue staining

201 (SimplyBlue™ SafeStain, Life Technologies) or sent to Taplin Mass Spectrometry Facility at
202 Harvard Medical school for protein identification from SDS-PAGE gel (Supplementary Table 1).
203 In preparation of protein extracts for pull-down experiments with MDCK cells: one 75 mm
204 flask of MDCK or MDCK *AF-6*$^{-/-}$ cells polarized for three days was lysed in 180 µL of cell lytic M
205 supplemented with complete Protease Inhibitor Cocktail (Roche). The soluble fraction was split in
206 two and incubated overnight under constant agitation with 20 µL of GST-Glutathione Sepharose™
207 4B or GST-InlP/2027/ΔLRR5/ΔLRR7/- Glutathione Sepharose™ 4B respectively (prepared
208 previously). The day after beads were washed with 2 mL of Tris-HCl 50 mM, NaCl 50 mM, free
209 glutathione 10 mM, pH 8.0. The bound proteins were eluted by boiling the beads in SDS sample
210 buffer (NuPAGE® sample reducing agent 10X and NuPAGE® LDS sample buffer 4X) for 30
211 min and analyzed by Western Blot or Coomassie blue staining (SimplyBlue™ SafeStain, Life
212 Technologies).
213 To detect afadin by Western Blot analysis, elution fractions were analyzed on 4-12% gels
214 (NuPAGE™ Novex™ 4-12% Bis-Tris Protein Gels) run on ice in MOPS buffer (NuPAGE®
215 MOPS SDS Running Buffer) for 3 h at 200 V and transfer was performed at 100V for 2 h.
216 Primary staining using mouse anti-afadin antibody (BD Transduction Laboratories™ , 1:2000) and
217 mouse anti- β-actin antibody (SIGMA, 1:1000) were incubated overnight at 4 °C. Secondary
218 antibody goat anti-mouse IgG-HRP (1:10000, Santa Cruz Biotechnology's) was incubated for 1 h
219 at room temperature. Protein detection was performed using ECL Western Blotting Substrate™
220 (Pierce).
221
222 **Human tissue collection and immunofluorescence.** For human placental organ cultures,
223 placentas from elective terminations of pregnancy (gestational age 4 to 8 weeks) were collected

224 and prepared as previously described (30). Briefly, fragments from the surface of the placenta
225 were dissected into 3-6 mm tree-like villi, placed on Matrigel (BD Biosciences)-coated Transwell
226 filters (Millipore, 30-mm diameter, 0.4 μm pore size) and cultured in Dulbecco's modified Eagle-
227 F12 medium (DMEM-F12; 1:1, vol/vol) supplemented with 20% FBS, 1% L-glutamine and 1%
228 penicillin/streptomycin (Invitrogen). Organ cultures were fixed for 15-30 min in 4%
229 paraformaldehyde at room temperature, flash frozen in Tissue-Tek O.C.T. Compound (Sakura
230 Finetek, Torrance, CA). Sections were cut at 7 μM, permeabilized for 5 min in ice-cold acetone,
231 dried, rehydrated in PBS, and blocked with Background Buster (Innovex Biosciences, Richmond,
232 CA). Primary staining with mouse anti-afadin antibody (BD Transduction Laboratories™ , 1:2000)
233 was incubated for 2 h at room temperature in PBS with 1% BSA and 5% normal goat serum
234 (Jackson ImmunoResearch Laboratories). Secondary staining with Alexa-Fluor® 594 goat anti-
235 mouse (1:500, ThermoFisher Scientific) was incubated for 1 h at room temperature, nuclei stained
236 with DAPI (Affymetrix), and sections mounted in Vectashield Mounting Medium (Vector
237 Laboratories). Stitched high-power images were acquired on a Nikon Ti-E epifluorescent
238 microscope with DS-Ri2 camera and NIS-Elements 4.30 software (Nikon Corporation).
239
240 **Mammalian cell line tissue culture.** MDCK (Madin Darby Canine kidney cell line,
241 ATCC), MDCK-AF6^{-} (a generous gift from Denise Marciano, UT Southwestern) cells were
242 grown in Eagle's MEM (Minimal Essential Medium) with Earle's Balanced Salt Solution (BSS)
243 supplemented with 10% FBS. Invasion assays and growth curves were performed as previously
244 described (31). MDCK cells expressing a humanized version of InlP were generated as follows:
245 the IRES-GFP sequence was amplified from the pIRES-EGFP-puro plasmid (Addgene) using
246 oligo fw-IRESGFP-EcoRI: GGAATTCGAATTCTAAGCCCCTCTCCCTCCCCCC and rv-

247 IRESGFP-BamHI GGAATTCGGATCCTTACTTGTACAGCTC GTCCATGCCG and cloned
248 into the plasmid PCR2.1. The *inlP* gene was codon optimized for expression in mammalian cells
249 (h*inlP*) and the NheI-h*inlP*-Flag-EcoRI construct was synthesized by GeneWiz. Using the
250 restriction enzymes NheI and EcoRI the NheI-h*inlP*-Flag-EcoRI construct was then cloned into
251 PCR2.1-IRES-GFP. The construct NheI-h*inlP*-Flag-EcoRI-IRES-GFP-BamHI was then cut from
252 PCR2.1 using the restriction enzymes NheI-BamHI and cloned in pCW-Cas9-Blast (Addgene)
253 plasmid by replacing the Cas9 gene and generating the plasmid pCW- h*inlP*-Flag-IRES-GFP.
254 UCSF ViraCore (http://viracore.ucsf.edu/) was used to generate a Lentivirus strain carrying pCW-
255 h*inlP*-Flag-IRES-GFP, which was used to transduce MDCK or MDCK *AF-6*$^{-/-}$ cells. Viral
256 transduction was performed in 12-well plates as follows: freshly plated MDCK cells were allowed
257 to adhere for 1 h at 37 °C ($4x10^4$ cells/well), next nearly all media was removed and 350 µl of viral
258 supernatant was added to each well, followed by overnight incubation at 37 °C. The next morning
259 1 mL fresh media was added to each well without removing the viral supernatant and cells were
260 grown for 48-72 h, followed by puromycin selection (5 µg/mL) for another 4 days. Protein
261 expression was analyzed by Western Blot +/- addition of doxycycline 1 µg/mL. Primary staining:
262 mouse anti-flag antibody (1:5000), and mouse anti-β-actin antibody (SIGMA, 1:1000), secondary
263 antibody: goat anti-mouse IgG-HRP (1:10000, Santa Cruz Biotechnology). Protein detection was
264 performed using ECL Western Blotting Substrate™ (Pierce).
265
266 **Traction force microscopy (TFM).** Single cell TFM assays were performed as previously
267 described (32, 33). Two layered polyacrylamide hydrogels, the upper of which contained 0.04%
268 carboxylate-modified red latex beads of 0.1 µm in diameter (FluoSpheres; Molecular Probes)
269 were prepared and activated via SulfoSanpah crosslinker (Thermo Fischer Scientific, 22589) as

270 previously described (32, 33). Hydrogels were attached to 24-well glass bottom plates (MatTek)
271 to enable monitoring of multiple conditions simultaneously. The stiffness of the hydrogels was
272 5 kPa, achieved with a 5% final concentration of acrylamide (Sigma, A4058) and 0.15% final
273 concentration of bis-acrylamide (Fisher, BP1404-250). Activated hydrogels were coated with
274 collagen I (Sigma-Aldrich, C3867) overnight at 4 °C. Hydrogels were washed with PBS the next
275 day and equilibrated with cell media for 30 min at 37 °C prior to addition of cells.

276 For single cell TFM experiments, 2 mL containing $10x10^5$ cells were added on six-well TC
277 polystyrene plates for 24 h. Upon seeding 1 μg/mL doxycycline was added to the wells where InlP
278 expression was desired. The next day, cells were lifted via 0.25% trypsin-EDTA, washed once in
279 PBS and then cell pellets were re-suspended in media and $0.5x10^4$ cells in 1 mL were added per
280 hydrogel to achieve single cell attachment. Cells were allowed to adhere for 3 h at 37 °C before
281 imaging. To measure cell-ECM traction forces in confluent monolayers cells were added to a
282 concentration of $4x10^5$ cells per well directly onto the hydrogels 24 h prior to imaging. Upon
283 seeding 1 μg/mL doxycycline was added to the wells where InlP expression was desired.

284 Multi-channel time-lapse sequences of fluorescence (to image the beads within the upper
285 portion of the hydrogels) and phase contrast images (to image the cells) were acquired using an
286 inverted Nikon Diaphot 200 with a CCD camera (Andor Technologies) using a 40X Plan Fluor
287 NA 0.60 objective and the MicroManager software package (Open Imaging). In addition, at the
288 beginning and end of the recordings an image of the cells' nuclei stained with 1 μg/mL Hoechst
289 and an image of InlP fluorescence were acquired to ensure similar cell densities and similar InlP
290 expression across conditions, respectively. The microscope was surrounded by a cage incubator
291 (Haison) maintained at 37 °C and 5% CO_2. Images were acquired every 5 min for approximately 4
292 h. Subsequently, at each time interval we measured the 2D deformation of the substrate at each

293 point using an image correlation technique similar to particle image velocimetry (34). We
294 calculated the local deformation vector by performing image correlation between each image and
295 an undeformed reference image which we acquired by adding 10% SDS at the end of each
296 recording to detach the cells from the hydrogels. We used interrogation windows of 32 x 16 pixels
297 (window size x window overlap) for cells forming a monolayer or 32 x 8 pixels for single cells.
298 For single cell experiments, we used a custom algorithm using MATLAB (MathWorks) to
299 identify the contour of the cells from the phase contrast images (35). We calculated the two-
300 dimensional traction stresses that single cells exert to the hydrogel as described elsewhere (35).
301 We calculated the strain energy (U_s) as the mechanical work imparted by the cell to deform its
302 hydrogel:
303 $U_s = \frac{1}{2}\int_s \vec{\tau}(z=h)\cdot\vec{u}(z=h)\,ds$, where $\vec{u}$ is the measured displacement vector field on the free
304 surface of the hydrogel and $\int_s ()\,ds$ represents a surface integral. For cell monolayer experiments,
305 traction stresses were measured as described above and elsewhere (33, 36).
306
307 ***In vitro* transcytosis and invasion assays.** To quantify *L. monocytogenes* transcytosis,
308 MDCK cells were seeded on Transwell™ inserts with a 3-μm pore size loaded onto tissue culture-
309 treated 12-well plates (Corning, 3402) at a density of 5×10^5 cells per insert three days prior to
310 infection. The day before infection, *L. monocytogenes* cultures were inoculated in 3 mL of Brain
311 Heart Infusion (BHI) directly from glycerol stocks and grown at 30 °C for 15 to 16 h without
312 agitation. The day of the experiment, the optical density of the overnight cultures was measured to
313 ensure that the MDCK cells were infected with a comparable multiplicity of infection (MOI)
314 across bacterial strains. For each strain, 1.2 mL was centrifuged at 2000 x g for 5 min, and washed
315 with 1 mL of DPBS. Bacterial pellets were resuspended in 16 mL of MEM. Host cells were

316 washed with MEM once, infected with 0.5 mL of bacterial mix per Transwell, and incubated at 37
317 °C for 10 min. The unused bacterial mix was serially diluted and plated onto BHI agar plates
318 containing 200 μg/mL streptomycin for bacterial enumeration. Transwells were washed three
319 times with MEM alone, then basal and apical media were both replaced with MEM + 10% FBS,
320 and plates were incubated at 37 °C for 1 h to allow bacterial invasion, followed by replacement
321 with MEM + 10% FBS + 50 μg/mL gentamicin to kill extracellular bacteria, and incubated at 37
322 °C for 15 min more. To assess subsequent transcytosis, Transwells were washed three times with
323 MEM + 10% FBS, and were then transferred to a new 12-well plate containing 1 mL of fresh
324 MEM + 10% FBS per well. This plate was incubated at 37 °C for 1 h, at which point basal media
325 was collected, vortex vigorously and 100 μL of each sample plated onto BHI agar plates
326 containing 200 μg/mL streptomycin. This step served as a negative control to exclude for
327 damaged monolayers. Meanwhile, the Transwells were transferred to another new 12-well plate
328 containing fresh MEM + 10% FBS per well. After an additional 3 h at 37 °C, basal media was
329 plated on BHI agar plates containing 200 μg/mL streptomycin as before, this time to assess true
330 transcytosis.

331 To quantify *L. monocytogenes* invasion, MDCK cells were seeded onto tissue culture-
332 treated 12-well plates at a density of 5×10^5 cells per well three days prior to infection. MDCK cells
333 were then infected with an Δ*actA L. monocytogenes* strain expressing mTagRFP under the actA
334 promoter (37), which becomes transcriptionally active upon entry into the host cell cytoplasm.
335 Invasion was assayed with flow cytometry as previously described (38).

336 **RESULTS**

337 ***InlP binds afadin***

338 We attempted to find host binding partners for InlP in placental cells using a yeast two-
339 hybrid system to screen a human placenta library (39) (Supplementary Table 1). In parallel, we
340 used InlP fused to glutathione-S-transferase (InlP-GST) and a mass spectrometric approach to
341 pull-down and identify InlP binding partners in human placental tissue extracts (Supplementary
342 Fig. 1 and Supplementary Table 2). Both methods should in principle be able to detect both host
343 cell surface and cytoplasmic binding partners for InlP. While each of these approaches identified
344 multiple candidates, the protein afadin, encoded by the *MLLT4/AF-6* gene, was the only one
345 identified by both. Afadin is an F-actin-binding protein that also binds to the cytoplasmic domain
346 of the cell-cell adhesion molecule nectin, as well as to a wide variety of signaling proteins
347 including Src and multiple members of the Ras superfamily (40). Afadin has been shown to
348 contribute to the formation of cell-cell junctions during mouse embryonic development (41, 42)
349 and to apical constriction of adherens junctions during *Drosophila* morphogenesis (43). In
350 addition, afadin has been proposed to play multiple roles in cell polarization, migration,
351 differentiation, and oncogenesis (40).

352 We confirmed specific binding of InlP to afadin by pull-down experiments followed by
353 Western blot analyses (Fig. 1A and 1B). Elution fractions obtained after pull-down using an InlP-
354 GST fusion protein incubated with cell lysates from MDCK, MDCK *AF-6*$^{-/-}$ or human placental
355 villi were analyzed. Using anti-afadin antibodies, we detected afadin signal in the input fraction
356 and in the elution fractions after incubation of InlP-GST with protein extract from MDCK cell
357 lines (Fig. 1A) or from human placental villi (Fig. 1B). No afadin was detected in the elution
358 fractions when the GST control was used as bait (Fig. 1A and 1B). Confirming the specificity of

359 our antibodies, Western blot analysis on pull-down experiments performed using protein extract
360 from the afadin knock-out MDCK cell line did not show a detectable signal (Fig. 1A).
361 To determine the amount and spatial distribution of afadin present in human placental villi,
362 we performed immunofluorescence microscopy staining for afadin and observed that this protein
363 is very abundant in the placenta (Fig. 1C). Localization was primarily observed at the CTB layer
364 just beneath the syncytium, with small amounts in the stroma (see asterisk and arrow in Fig. 1C).
365 The high abundance of this potential InlP binding partner in the placenta, combined with our
366 previous report that InlP plays an important role in *L. monocytogenes* infection at the maternal-
367 fetal interface (1), are consistent with the hypothesis that InlP-afadin interactions are important for
368 the pathogenesis of placental infections.
369
370 ***Lmo2027 is a structural paralog of InlP that does not bind afadin***
371 The internalins that are predicted to be secreted by *L. monocytogenes* include InlC
372 (Lmo1786), InlP (Lmo2470), Lmo2027 and Lmo2445 (24). Of these, only InlC has been
373 extensively studied, but its primary sequence is not particularly similar to that of InlP (24%
374 sequence identity). The two other internalins predicted to be secreted, Lmo2027 and Lmo2445,
375 have not yet been characterized. Pairwise analyses of amino acid sequences indicated that InlP and
376 Lmo2445 are only 25% identical and 40% similar; however, InlP and Lmo2027 are much less
377 divergent, with 65% identity and 77% similarity (Fig 2A). Moreover, InlP and Lmo2027 share a
378 similar C-terminal domain that is not found in any of the other internalin family members (24).
379 Because of its high degree of sequence similarity to InlP, we decided to test whether Lmo2027
380 also binds afadin. As before, we performed pull-down assays with MDCK cell lysates, followed by
381 Western blots on elution fractions using Lmo2027-GST or InlP-GST fusion proteins as bait (Fig.

382 2B, C). Unlike InlP-GST, Lmo2027-GST did not enrich the afadin signal in the elution fractions
383 significantly more than the GST control. Even when diluted 10-fold, InlP-GST still pulled down
384 considerable afadin in comparison to the GST control and Lmo2027-GST. These results show that,
385 despite the relatively high sequence similarity of the two proteins, InlP, but not Lmo2027, binds
386 afadin.

387 To identify structural distinctions that might account for differences in afadin binding
388 affinity, we obtained 1.4 Å and 2.3 Å crystal structures of InlP and Lmo2027, respectively
389 (Supplementary Table 3). Analysis of the structures reveals that InlP and Lmo2027 generally
390 resemble previously characterized internalins (Fig 2D, E). Both proteins possess an N-terminal
391 domain that adopts the helical structure characteristic of internalins. This is followed by a concave
392 leucine rich-repeat (LRR) domain made up of 9 LRRs in InlP and 8 LRRs in Lmo2027 that can be
393 further subdivided into a "cryptic" portion consisting of 3 LRRs, which were not anticipated to
394 adopt an LRR-fold based upon bioinformatics analyses, and a "canonical" portion consisting of 6
395 LRRs in InlP and 5 LRRs in Lmo2027. Finally, the C-terminal domain in both proteins assumes
396 an immunoglobulin-like fold.

397 In particular, two features distinguish InlP and Lmo2027 from each other and from
398 previously characterized internalins. First, the additional LRR in InlP extends the LRR domain in
399 this protein as compared to Lmo2027 and increases the distance between the N-terminal and Ig-
400 like domains by ~4 Å. Such a fundamental distinction in the dimensions of the internalin could
401 affect whether a prospective binding partner could dock to and bind the LRR. Second, the concave
402 surface of previously crystallized internalin LRRs present an unbroken β-sheet (24), but in InlP
403 and Lmo2027 the third cryptic LRR (3rd LRR loop) protrudes, adopting a twisted conformation
404 that disrupts the continuity of this surface. Since this region in other LRR proteins is generally

405 involved in engaging the protein binding partner (22, 44), the distinct 3rd LRR loop seems well
406 situated to play a role in conferring binding specificity.
407 Unexpectedly, a calcium ion (from the crystallization solution) bound to the center of the
408 3rd LRR loop structure in InlP, but not Lmo2027 (Fig. 2D, E; Supplementary Fig. 2A), suggesting
409 that a calcium-stabilized loop conformation might be relevant for InlP protein-protein interactions.
410 Two of the residues specifically involved in coordination of the calcium ion in the InlP crystal
411 structure, D132 and G135, are not conserved in Lmo2027 (changed to T and E respectively). To
412 examine the interaction between InlP and calcium, we performed isothermal calorimetry
413 experiments, and found that calcium binds with a relatively low affinity of 35 μM (Supplementary
414 Fig. 2B).
415
416 ***InlPΔLRR5 has reduced afadin binding affinity***
417 Based on the alignment shown in Fig. 2A, it is evident that the main differences between
418 InlP and Lmo2027 are amino acid differences in that cluster to the C-terminal domain, as well as
419 the absence of 22 amino acid residues of Lmo2027 corresponding to one of the LRR motifs of
420 InlP. Given the high sequence similarity of the 6 "canonical" LRR motifs, it is difficult to
421 definitively identify which one is missing in Lmo2027, even if the pairwise alignment between
422 InlP and Lmo2027 suggests that the missing LRR motif might be LRR7. Therefore, we decided to
423 systematically delete individual LRR motifs in the InlP protein and test the effect of these
424 deletions on the protein's ability to bind afadin. We successfully generated three InlP deletion
425 mutants—InlPΔLRR5-GST, InlPΔLRR7-GST and InlPΔLRR8-GST—lacking the LRR5 (Δamino
426 acids 174-195), the LRR7 (Δamino acids 218-239) and the LRR8 (Δamino acids 240-261) motifs,

427 respectively. Each of these was then used as bait in pull-down experiments with MDCK cell
428 lysates, followed by Western blot analysis of the elution fractions to detect afadin.
429 Resins prepared using *E. coli* lysate expressing InlPΔLRR7-GST (Fig. 3A) pulled down
430 afadin from MDCK cell lysates with an efficiency roughly comparable to that observed for InlP-
431 GST (Fig. 3B). In contrast, we detected lower amounts of afadin in the pull-down fraction when
432 lysate from *E. coli* expressing the InlPΔLRR5-GST fusion protein was used to prepare the resin
433 (Fig. 3B). As the expression level of the InlPΔLRR5-GST fusion protein in *E. coli* appeared to be
434 somewhat lower than that of either InlP-GST or GST alone (Fig. 3A), we also performed a
435 Western blot comparing the elution fractions after five-fold dilution for both InlP-GST and GST
436 with no dilution for the InlPΔLRR5-GST elution fraction. Even compared to diluted InlP-GST,
437 substantially less afadin was detected in the sample for InlPΔLRR5-GST (Fig. 3C). This suggests
438 that deletion of the LRR5 motif decreases the affinity of afadin by at least ten-fold. The solubility
439 of the InlPΔLRR5-GST recombinant fusion protein was confirmed by dynamic light scattering
440 analysis (data not shown), consistent with the hypothesis that this reduction in apparent binding
441 affinity is due to specific structural alterations in the LRR domain. The InlPΔLRR8-GST was
442 expressed in *E. coli* lysates at ~30% of InlP-GST levels prepared under similar conditions
443 (Supplementary Fig. 3A). While we did observe reduced afadin binding by resins prepared using
444 *E. coli* lysates containing this fusion protein as compared to native InlP-GST (Supplementary Fig.
445 3B), this decrease was approximately proportional to the reduction in expression level. Overall
446 this analysis suggested that InlPΔLRR5 represents a useful mutant for interrogating the InlP-
447 Afadin interaction.
448 To examine the effects of the InlPΔLRR5 mutation on binding to host proteins, we used a
449 GST control, InlP fused to GST (InlP-GST), InlPΔLRR5 fused to GST (InlPΔLRR5-GST), or

450 Lmo2027 fused to GST (Lmo2027-GST) as bait and identified proteins pulled down from MDCK
451 lysates by mass spectrometry (Supplementary Table 4). Of the MDCK cell proteins found
452 specifically bind InlP-GST, only afadin (*MLLT4/AF-6*) had also been identified in the screens
453 described above using yeast two-hybrid screening on a human placental library (Supplementary
454 Table 1) and mass spectrometry of proteins pulled down from human placental tissue extracts
455 (Supplementary Table 2). Consistent with the Western blot analysis, mass spectrometry confirmed
456 that afadin associated much less strongly with InlPΔLRR5-GST or Lmo2027-GST than with InlP-
457 GST. Several proteins were also identified that were pulled down with approximately similar
458 efficiency by both InlP-GST and InlPΔLRR5-GST, but not Lmo2027-GST, as were several others
459 pulled down with similar efficiency by all three recombinant fusion protein baits (Supplementary
460 Table 4). These findings are consistent with the hypothesis that the InlPΔLRR5 mutant is
461 specifically deficient in interacting with afadin in MDCK cells, while otherwise retaining much of
462 its normal structure and protein-protein interaction potential.
463
464 ***Afadin-InlP interactions decrease the attachment of epithelial cells to the extracellular matrix,***
465 ***but not adhesion between adjacent epithelial cells***
466 We sought to investigate whether the interaction between InlP and afadin could alter the
467 structural integrity of epithelial cell monolayers in ways that might facilitate *L. monocytogenes*
468 invasion or cell-to-cell spread. To test whether InlP affects the integrity of cell-cell junctions in a
469 monolayer, we constructed a line of MDCK cells that could express a humanized version of InlP
470 (hInlP) after induction by doxycycline (MDCK-hInlP^{+}). We cultured wild-type MDCK, MDCK
471 *AF-6*$^{-/-}$, and MDCK-hInlP cells on Transwell filters for three days and measured the permeability of
472 the cell monolayers using inulin-FITC. As expected after deletion of a protein necessary for

473 proper formation of adherens junctions and tight junctions (41), MDCK *AF-6*$^{-/-}$ monolayers showed
474 a substantial increase in permeability to inulin relative to wild-type MDCK monolayers. However,
475 MDCK-InlP monolayers showed low permeability, comparable to the baseline level for wild-type
476 MDCK monolayers, both with and without induction of the hInlP transgene using doxycycline
477 (Fig. 4A). This result suggests that the interaction between InlP and afadin does not inhibit the
478 ability of afadin to perform its normal function in establishment and maintenance of impermeable
479 cell-cell junctions.

480 Next, we used these cell lines to examine the modulation of cell-substrate interactions by
481 InlP binding to afadin. To this end, we also generated a line of MDCK *AF-6*$^{-/-}$ cells with the
482 doxycycline-inducible hInlP transgene. We used traction force microscopy (TFM) to measure the
483 ability of MDCK cells to generate traction forces on their substrates with and without expression
484 of Afadin and/or InlP. Uninduced MDCK-hInlP cell monolayers without doxycycline (the
485 positive control) grown on deformable substrates as confluent, polarized monolayers were able to
486 generate significant strain energy on the order of 100-200 nN·μm (Fig. 4B, C) and to exert
487 traction stresses with peak values around 100 Pa, comparable to previous reports (45, 46). Both
488 the induction of the hInlP transgene and the deletion of afadin caused a substantial reduction in
489 strain energy. Induction of hInlP expression in the background of the MDCK *AF-6*$^{-/-}$ cell line did
490 not lead to any further reduction, consistent with the hypothesis that the primary effect of InlP
491 expression on abrogation of traction force generation in MDCK cells is due to its interaction with
492 afadin.

493 We have previously demonstrated that a decrease in monolayer traction force can be
494 caused either by a direct inhibition of cell-substrate interactions or by an indirect inhibition of
495 lateral tension at cell-cell junctions in the monolayer (33). To distinguish between these two

496 possibilities, we also performed TFM for isolated cells under the same four conditions. Just as for
497 the monolayers, either the expression of InlP or the deletion of *AF-6* caused a significant decrease
498 in the ability of isolated individual cells to generate traction force (Fig. 4D, E). Taken together,
499 these results suggest that the InlP-afadin binding interaction specifically disrupts afadin's normal
500 activity in enhancing traction force generation at the cell-substrate interface, but has no effect on
501 afadin's normal function at cell-cell junctions in the monolayer.
502
503 ***InlP enhances L. monocytogenes transcytosis through MDCK polarized monolayers***
504 Finally, we examined the influence of the InlP-afadin interaction on infection and spread
505 of *L. monocytogenes* in MDCK monolayers. We infected wild-type and MDCK *AF-6*$^{-/-}$ cells with
506 wild type or *ΔinlP L. monocytogenes*. Gentamicin was added at 30 min to kill extracellular
507 bacteria, and remaining intracellular bacteria were enumerated at 2, 5, 8 and 24 h post-infection.
508 At 2 h, the MDCK *AF-6*$^{-/-}$ cells harbored ~10 times the number of bacteria as compared to wild-
509 type MDCK cells, although the rate of intracellular growth of the bacteria was unchanged.
510 Deletion of *inlP* had no significant effect on invasion or intracellular replication of *L.*
511 *monocytogenes* in either host cell background (Fig. 5A).
512 The observation that MDCK *AF-6*$^{-/-}$ monolayers had substantially more intracellular
513 bacteria at early time points in the course of infection as compared to wild-type MDCK cells
514 raised the possibility that the deletion of *AF-6* caused an increase in the efficiency of *L.*
515 *monocytogenes* invasion. Because the cell receptor for *L. monocytogenes* invasion into epithelial
516 cells, E-cadherin, is normally sequestered from the apical surface of cells in well-polarized,
517 confluent monolayers, invasion under such circumstances is rare and typically takes place at sites
518 of local, transient disruption of the epithelial cell-cell junctions, for example at sites of extrusion

519 of apoptotic cells (8). Consequently, any disruption of normal cell-cell junctions in epithelial
520 monolayers typically increases the efficiency of *L. monocytogenes* invasion (38). To determine if
521 this was the reason for the increased bacterial load in MDCK *AF-6*$^{-/-}$ monolayers at early time
522 points, we infected both wild-type and *AF-6*-knockout MDCK cells with Δ*actA L. monocytogenes*
523 expressing mTagRFP under the *actA* promoter and counted the number of RFP-positive host cells
524 by flow cytometry 5 h post-inoculation, which represents the number of bacteria-containing cells.
525 Because these bacteria are not capable of actin-based cell-to-cell spread, this assay allows
526 determination of the number of directly invaded host cells, independent of any later variations in
527 bacterial spread (47). Indeed, we found approximately 6-fold more invasion of MDCK *AF-6*$^{-/-}$ cells
528 with *L. monocytogenes* as compared to wild-type MDCKs (Fig. 5B).

529 Our previous work demonstrated that wild-type and *ΔinlP L. monocytogenes* form foci of
530 similar size in MDCK monolayers (1), suggesting that horizontal cell-to-cell spread in a polarized
531 epithelium is not affected by InlP. This is corroborated by our findings here that the InlP-afadin
532 interaction does not disrupt the function of afadin at cell-cell junctions. However, we also showed
533 that *ΔinlP* strains are impaired in spreading from the CTB epithelial layer into the placental
534 stroma (1), and here we have found that the InlP-afadin interaction specifically disrupts the
535 mechanics of MDCK cell traction force generation at the cell-substrate interface (Fig. 4). We
536 therefore wondered whether this protein-protein interaction might specifically affect the ability of
537 intracellular *L. monocytogenes* to use actin-based motility to spread through the basal face of the
538 CTB epithelial monolayer underlying the placental STB, rather than horizontally through the
539 lateral faces of neighboring CTB epithelial cells. We designed an assay to mimic this particular
540 type of spread by growing MDCK cells on Transwell filters with large (3 μm) pores through
541 which bacterial protrusions could extend into the lower well. Under these culture conditions,

542 MDCK cells form well-polarized monolayers and secrete a thick and well-organized basement
543 membrane (basal lamina) (48), so bacterial protrusions reaching the lower well must have been
544 able to form at the basal side of the cell and push through the basement membrane. Approximately
545 5 hours after inoculation from the apical side, bacteria that had successfully performed
546 transcytosis through the monolayer were collected from the lower well. In this assay, *ΔactA*
547 bacteria exhibited a substantial (>10-fold) reduction in transcytosis, demonstrating that this
548 process is dependent on bacterial actin-based motility (Fig. 5C). The *ΔinlP* strain also showed a
549 statistically significant reduction in transcytosis (~4-fold), consistent with the hypothesis that the
550 InlP-afadin interaction specifically alters cell mechanics at the basal cell-substrate interface and
551 thereby facilitates *L. monocytogenes* spread in a direction perpendicular to the monolayer.
552 If the nature of the InlP-afadin interaction were simply to sequester or inhibit afadin's
553 normal activity at the basal surface, we would expect that deletion of *AF-6* in the host cells should
554 be able to rescue the transcytosis defect of *ΔinlP L. monocytogenes*. Interestingly, however, this
555 was not the case. MDCK *AF-6*$^{-/-}$ monolayers infected with wild-type bacteria exhibited an
556 unexpected decrease in transcytosis efficiency, resulting in about two-fold fewer bacteria reaching
557 the lower well as compared to parallel infections in wild-type MDCK cells, despite the much
558 higher efficiency of initial invasion (Fig. 5C). In this host cell background, transcytosis of *ΔinlP*
559 bacteria was slightly less efficient than that of wild-type bacteria, in contrast to the expected
560 phenotypic rescue.
561 We wished to confirm that this unexpected observation could be attributed specifically to
562 the InlP-afadin interaction, rather than to some pleiotropic effect of *AF-6* deletion in the MDCK
563 cells, and so took advantage of our earlier determination that the InlPΔLRR5 mutation specifically
564 disrupts afadin binding (Fig. 3, Supplementary Table 4). Infection of wild-type MDCK cells with

565 *L. monocytogenes* expressing the mutant InlPΔLRR5 resulted in a transcytosis defect comparable
566 to the defect of the complete *ΔinlP* deletion in parallel experiments (Fig. 5D). We conclude that
567 the InlP-afadin protein-protein interaction exerts a specific effect to enhance transcytosis of *L.*
568 *monocytogenes* through the basal face of polarized epithelial cells that is not equivalent to the
569 simple removal or sequestration of afadin from this site.

570 **DISCUSSION**

571 En route to infection of the fetus, *L. monocytogenes* experiences multiple bottlenecks,
572 from trafficking to the placenta (3) to surviving the placental innate immune defenses (49) to
573 crossing the trophoblast monolayer and its associated basement membrane into the fetal stroma
574 and fetal circulation (20). InlP initially attracted our interest due to its identification in a screen for
575 *L. monocytogenes* mutants that were defective in their ability to infect the placenta (1). Two
576 unbiased screening methods to identify potential placental binding partners, a yeast two-hybrid
577 screen using a placental cDNA library and mass spectrometric identification of human proteins
578 pulled down by InlP from placental extracts, converged on afadin as a significant candidate
579 binding partner. Afadin is not found on the cell surface, but instead is primarily associated with
580 the cytoplasmic face of cell-cell junctions containing nectin (41, 53). Therefore, it seems likely
581 that InlP is most helpful in breaching that third barrier and accessing the fetal stroma.

582 Of the 25 known members of the *L. monocytogenes* internalin family, the only other one
583 known to have host cell cytoplasmic binding partners involved in its virulence functions is InlC.
584 InlC binds to one of the subunits of the IκB complex thereby modulating the host cell innate
585 immune response (54). In addition, InlC also binds the adapter protein Tuba, which cooperates
586 with the actin polymerization regulator N-WASP to modulate tension at cell-cell junctions and
587 thereby promote *L. monocytogenes* cell-to-cell spread in epithelial monolayers (55). Intriguingly,
588 InlC and InlP are two of only four internalin family members that are thought to be secreted in a
589 soluble form rather than anchored to the bacteria cell surface (24). As more internalin family
590 members are characterized, it will be interesting to see whether the trend persists of surface-
591 anchored internalins binding to host cell surface proteins and secreted internalins binding to host
592 cell cytoplasmic proteins.

593 While we have not determined the structure of the InlP-afadin complex, our work does
594 give some clues into the likely nature of this interaction. The internal in-frame deletion mutant
595 InlP-ΔLRR5, which lacks one of the leucine-rich repeats, binds afadin less well than full length
596 InlP, but this is probably not simply due to the shorter overall size of the concave face of the LRR
597 domain because InlP-ΔLRR7 and InlP-ΔLRR8, which should have a similar overall length of the
598 LRR domain concave face, seem to have little or no deficiency in afadin binding. It is thus likely
599 that there are specific residues in LRR5 that stabilize the interaction. An interesting unanswered
600 question concerns the role of the unusual protruding loop from LRR3 in determining binding
601 partner specificity. Although we found that this loop between amino acids 132-136 in the InlP
602 structure bound Ca^{2+} with an affinity of 35 μM, this binding affinity is probably too weak to be
603 relevant in the host cell cytoplasm where the Ca^{2+} concentration rarely rises above ~2 μM (56).
604 This is not the case for other subcellular compartments like the acidifying phagosomes, where the
605 Ca^{2+} concentration has been shown to be >70 μM (56). Thus, it is possible that calcium binding by
606 InlP plays a role during *L. monocytogenes* escape from the primary (single-membrane) or
607 secondary (double-membrane) vacuole. It should be noted that Shaughnessy et al. (57) observed
608 that listeriolysin O pores generated by the bacterium in the process of primary vacuolar escape
609 allow Ca^{2+} in the vacuole to leak into the cytoplasm, albeit slowly. It is possible that calcium
610 binding promotes changes in InlP behavior that are specific to different calcium microdomains in
611 the polarized epithelium (58, 59), including microdomains potentially specific to basal protrusions
612 and/or placental trophoblasts (60).
613 Other bacterial pathogens are also known to secrete virulence factors into the host cell
614 cytoplasm that modulate host cell biology in ways that benefit bacterial survival or spread (33, 61-
615 64). One particularly relevant example is the virulence factor Sca4, secreted by *Rickettsia parkeri*.

616 Analogous to InlC, Sca4 binds the host protein vinculin at cell-cell junctions and alters cortical
617 tension, promoting actin-based cell-to-cell spread of the bacterium horizontally through host cell
618 monolayers (33). Given the precedent that both InlC and Sca4 bind to proteins that perform
619 scaffolding functions at cell-cell junctions in polarized epithelia (Tuba and vinculin respectively)
620 and modulate cortical tension to promote bacterial spread, our initial expectation on discovering
621 that InlP binds the cell-cell junction-associated protein afadin was that its mechanism of action
622 would be similar. However, we have found no evidence that InlP has any effect on cell-cell
623 junctions in the host monolayer, or indeed that it makes any significant contribution to lateral
624 actin-based spread of *L. monocytogenes* within the horizontal plane of the monolayer.
625 Instead, our results indicate that the relevant site of action of InlP in the host cell is the
626 basal face, not the lateral face, and that the InlP-afadin interaction specifically modulates the
627 nature of the host cell organization at the basal face or interaction with the underlying basement
628 membrane in a way that promotes *L. monocytogenes* spread that is perpendicular, rather than
629 parallel to the monolayer. Afadin has not been described as being localized to the basal face of
630 polarized epithelial cells, or to cell-ECM junctions; instead its functional characterization has
631 focused primarily on nectin binding at cell-cell junctions (40, 41). Conditional knockouts in the
632 mouse intestine lead to increases in intestinal permeability (65), consistent with the phenotype we
633 have described here of afadin loss causing permeabilization of cell-cell junctions in MDCK cells.
634 Whether afadin also plays a role in cell-ECM connections is unclear, but in certain cell types,
635 removal of afadin can enhance cell migration (66) and invasive capacity (67), or suppress
636 neuronal axon branching (68). While these cellular behaviors might involve specific changes in
637 cell-ECM interactions, it is also likely in these cases that the effects of afadin disruption are

638 mediated indirectly through its interactions with critical signaling molecules, Rap1, Src and R-Ras
639 respectively (66-68).
640 How does InlP binding modulate afadin activity at the basal face of epithelial cells? For
641 both InlC and Sca4, deletion of the host cell binding partner is sufficient to (partially) rescue the
642 bacterial deletion phenotype, consistent with the simple idea that binding of the bacterial virulence
643 factors to their host cell partners effectively inhibits or sequesters those host cell partners (33, 55).
644 In contrast, our results indicate that the consequences of the interaction between InlP and afadin
645 are more complex than simple sequestration. InlP expression in uninfected MDCK cell
646 monolayers has no effect on integrity of cell-cell junctions, while deletion of afadin results in a
647 significant increase in monolayer permeability, so the presence of InlP does not appear to disrupt
648 afadin's normal activities at the cell-cell junctions. In contrast, expression of InlP phenocopies
649 afadin deletion with respect to the ability of epithelial cells to generate traction forces on their
650 substrates. And most intriguingly we have found that *AF-6* knockout MDCK cells are less able to
651 support transcytosis of both wild-type and *ΔinlP L. monocytogenes* across the basement
652 membrane than are wild-type host cells; if afadin normally simply strengthens the cell-substrate
653 interface then the *AF-6* knockout host cells should be more permissive for bacterial transcytosis,
654 rather than less. This raises the interesting possibility that the InlP-afadin binding interaction
655 results in a novel activity that specifically promotes bacterial formation of actin-based protrusions
656 at the cell basal face.
657 In the context of placental infection, the spatial specificity for the activity of the InlP-
658 afadin interaction at the basal face of polarized epithelial cells is relevant, as our previous work
659 has suggested that vertical spread from the CTB monolayer into the underlying fetal stroma is a
660 major barrier for infection of the fetus (1, 20, 69). However, we previously showed that the Δ*inlP*

661 mutant is not impaired in reaching the liver or spleen in orally-infected guinea pigs (1), raising the
662 question of why the phenotype is apparently specific for placental infection when enhanced
663 transcytosis through the basement membrane should also be relevant for *L. monocytogenes*
664 crossing the intestinal epithelium or crossing the endothelial cells in blood vessels to invade the
665 liver. In this context, we note that the intestinal barrier is organized differently from that of the
666 placenta. The intestinal epithelium is rich in intercellular junctions that link neighboring cells
667 together, while the placental syncytiotrophoblast that contacts maternal blood is a single,
668 continuous plasma membrane extending over tens of thousands of square millimeters in later
669 stages of human gestation. The invasive cytotrophoblasts in the uterine decidua do have exposed
670 lateral surfaces and cell-cell junctions, but they lack the lymphatic and immune components of the
671 intestine in that there are no Peyer's Patches and M cells with phagocytic and migratory
672 capabilities. While some white blood cells do traffic across this barrier in both directions (70),
673 traffic is likely more limited than in the mucosal-associated lymphoid tissues of the gut. The lack
674 of a role for InlP in crossing the intestinal barrier is therefore consistent with earlier work showing
675 that *L. monocytogenes* traffics from the gut to the bloodstream by being carried by immune cells
676 (71). In this context, the limited immune cell traffic observed across the placental barrier might
677 explain how *ΔinlP L. monocytogenes* are impaired in crossing the subsyncytial CTB monolayer—
678 undergirded by a basement membrane—into the fetal stroma (1). Alternatively, it is possible that
679 the basement membrane underlying the CTB layer simply presents a more formidable physical
680 barrier than that found underneath the intestinal epithelium. An interesting issue, to be addressed
681 in future work, is whether there is impairment in the invasion of *ΔinlP L. monocytogenes* across
682 the blood-brain endothelial barrier.

683 For decades, *L. monocytogenes* has been a useful tool for the study of mammalian cells,
684 barriers, and immune functions. Increasingly, its capacity to reveal basic knowledge about higher
685 levels of biological organization—mammalian tissues and organs—is becoming evident. Through
686 investigations of how bacteria cross barriers and of the interactions between bacterial factors and
687 host pathways, we learn not only more about what regulates pathogenesis, but about the structures
688 of these tissues themselves, in how they are generated, their composition, and how they can be
689 disrupted.

690 **AUTHOR CONTRIBUTIONS:**

691 C.F. and A.I.B. conceived the project and initiated collaborations with the other authors.
692 C.F. generated all bacterial mutant strains and mammalian cell lines. C.F., E.E.B., F.E.O., S.H.L.,
693 G.R., and S.N. performed experiments and/or analyzed data. W.F.A., J.A.T. and A.I.B. provided
694 resources and supervision. C.F., E.E.B., J.R.R., A.I.B. and J.A.T. wrote the paper.

695

696 **ACKNOWLEDGEMENTS:**

697 Our thanks to Henriette Macmillan, Cedric Brimacombe, George Minasov, Olga
698 Kiryukhina and Albin Cardona-Correa for discussions and experimental support, as well as tissue
699 donors who provided informed consent. This work was supported by NIH R01AI084928 (A.I.B),
700 Burroughs Wellcome Fund (A.I.B), NIH R01AI036929 (J.A.T), HHMI (J.A.T), the HHMI
701 Gilliam Fellowship for Advanced Study (F.E.O.), the Stanford Graduate Fellowship (F.E.O.), the
702 American Heart Association (E.E.B.), NIH F32AI108195 (G.R.), Society for Pediatric Pathology
703 Young Investigator Research grant (G.R.), and the University of California Partnerships for
704 Faculty Diversity President's Postdoctoral Fellowship (G.R.). Flow cytometry was performed at
705 the Stanford Shared FACS Facility. The Center for Structural Genomics of Infectious Diseases
706 has been funded with federal funds from the National Institute of Allergy and Infectious Diseases,
707 National Institutes of Health (NIH), Department of Health and Human Services, under Contract
708 Nos. HHSN272200700058C and HHSN272201200026C (to W.F.A). This research used resources
709 of the Advanced Photon Source, a U.S. Department of Energy (DOE) Office of Science User
710 Facility operated for the DOE Office of Science by Argonne National Laboratory under Contract
711 No. DE-AC02-06CH11357. Use of the LS-CAT Sector 21 was supported by the Michigan

Economic Development Corporation and the Michigan Technology Tri-Corridor (Grant 085P1000817).

715 **FIGURE LEGENDS**

716 **Figure 1. Bacterial effector InlP binds host adaptor protein afadin.** (A-B) InlP-GST fusion
717 protein (InlP) or GST protein alone (-) bound to glutathione-Sepharose resin were incubated
718 overnight with protein extracts from (A) MDCK or MDCK *AF-6*$^{-/-}$ cells or (B) human placenta.
719 Input (IN) and elution fractions (EF) were analyzed by Western blot with anti-afadin antibodies.
720 Actin: loading control. (C) Immunofluorescence of human placental villi stained for afadin (red)
721 and DAPI (blue), white bar =10 μm (right). Asterisk labels a portion of the stroma, and the arrow
722 points to some of the CTBs.

723

724 **Figure 2. Distinct features of InlP as compared to Lmo2027.** (A) Pairwise sequence alignment
725 of InlP and Lmo2027 with conserved amino acids highlighted in red. The LRRs and calcium
726 binding site on InlP are noted. Arrows signify ß-sheets and coils correspond to α-helices. (B)
727 Loading control of pull down experiments on Lmo2027 by Coomassie blue staining. GST protein
728 alone (-), Lmo2027-GST fusion protein (2027) or InlP-GST fusion protein (InlP) bound to
729 glutathione-Sepharose resin used as bait for pull-down experiments with protein extracts from
730 MDCK cells. The elution fraction from pull-down samples using InlP-GST (InlP) as bait were
731 sequentially diluted 5-fold before SDS analysis; undiluted elution fractions were analyzed from
732 pull-down samples using GST (-) or Lmo2027 (2027). Data shown are Coomassie staining and the
733 most abundant band in each lane represents the bait. (C) GST fusion proteins or GST protein
734 alone (-) bound to glutathione-Sepharose resin were incubated overnight with protein extracts
735 from MDCK cells, and elution fractions were analyzed by Western blot with anti-afadin
736 antibodies. The following GST fusion proteins were used: GST-Lmo2027 (Lmo2027) and GST-
737 InlP (InlP). Undiluted elution fractions were analyzed with the exception of the elution fractions

738 marked by black triangles: elution fractions from the experiments using GST-InlP as bait were
739 sequentially diluted by 5-fold before western blot analysis. Actin: loading control. (D) Crystal
740 structure of InlP with schematic depiction of domain layout below. (E) Crystal structure of
741 Lmo2027 with color-coded domains, like in (D).
742
743 **Figure 3. LRR5 stabilized afadin- InlP interaction.** (A) Loading control of InlP-afadin binding
744 pull-down experiments with LRR mutants by Coomassie blue staining. GST protein alone (-),
745 InlPΔLRR5-GST fusion protein (ΔLRR5), InlPΔLRR7-GST fusion protein (ΔLRR7), or InlP-GST
746 (InlP) bound to glutathione-Sepharose resin were used as bait for pull-down experiments with
747 protein extracts from MDCK cell line. Data shown are Coomassie staining, and the most abundant
748 band in each lane represents the bait. (B-C) GST fusion proteins or GST protein alone (-) bound to
749 glutathione-sepharose resin were incubated overnight with protein extracts from MDCK cells, and
750 elution fractions (EF) were analyzed by Western blot with anti-afadin antibodies. The following
751 GST fusion proteins were used: GST-InlP (InlP) and GST-InlP with deletions in LRR5 (ΔLRR5)
752 or LRR7 (ΔLRR7). Actin: loading control. Undiluted elution fractions were analyzed with the
753 exception of the elution fractions marked in panel C that were diluted 5-fold. Actin: loading
754 control.
755
756 **Figure 4. Cell-ECM traction stresses decrease in magnitude when afadin is not expressed or**
757 **when InlP is present.** (A) MDCK, MDCK *AF-6*$^{-/-}$, and MDCK cell lines stably transfected with
758 h*inlP* under a doxycycline (DOX) inducible promoter were grown on Transwell filters for three
759 days until formation of polarized epithelia. Inulin-FITC was added to the upper compartment of
760 the Transwell insert. The cell permeability was analyzed at different time points by measuring the

761 fluorescence intensity in the lower compartment. MDCK hInlP$^-$ and MDCK hInlP$^+$: stably
762 transfected cells without or with hInlP expression secondary to doxycycline exposure for 24 h
763 prior to the addition of Inulin-FITC. (B) Representative phase images (first row) and maps
764 showing the magnitude of traction stresses of confluent MDCK monolayers adherent to hydrogels
765 coated with collagen I (color indicates stress magnitude in Pa). Columns refer to: MDCK hInlP$^-$,
766 MDCK hInlP$^+$, MDCK *AF-6*$^-$/$^-$ hInlP$^-$ and MDCK *AF-6*$^-$/$^-$ hInlP$^+$. Scale bar corresponds to 20 µm.
767 (C) Time-averaged strain energy (nN•µm) calculated for multiple regions within confluent
768 MDCK monolayers. Boxplots refer to N=11 MDCK hInlP$^-$, N=11 MDCK hInlP$^+$, N=12 MDCK
769 *AF-6*$^-$/$^-$ hInlP$^-$, N= 12 MDCK *AF-6*$^-$/$^-$ hInlP$^+$ monolayer regions. (D-E) TFM results for single cells
770 adherent to polyacrylamide hydrogels coated with collagen I. (D) Instantaneous maps showing the
771 magnitude of traction stresses (color indicates stress values in Pa). Columns refer to: MDCK
772 hInlP$^-$, MDCK hInlP$^+$, MDCK *AF-6*$^-$/$^-$ hInlP$^-$ and MDCK *AF-6*$^-$/$^-$ hnlP$^+$. Cell outlines are in white.
773 Scale bar corresponds to 20 µm. (E) Time-averaged strain energy (nNµm) from individual cells.
774 Boxplots refer to N=15 MDCK hInlP$^-$, N=17 MDCK hInlP$^+$, N= 15 MDCK *AF-6*$^-$/$^-$ hInlP$^-$, and
775 N=18 MDCK *AF-6*$^-$/$^-$ hInlP$^+$. For boxplots in (C), (E) circles represent outliers, and the boxplots'
776 notched sections show the 95% confidence interval around the median (Wilcoxon–Mann–
777 Whitney test). One or two asterisks denote statistically significant differences between the
778 medians of two distributions (<0.05 or <0.01, respectively; Wilcoxon rank sum test).
779
780 **Figure 5. InlP enhances transcytosis through MDCK polarized monolayers**. (A) Intracellular
781 growth curves of wild type 10403S *L. monocytogenes* in MDCK (black solid line) or MDCK *AF-*
782 *6*$^{-/-}$ (black dashed line) cells and of Δ*inlP L. monocytogenes* in MDCK (gray solid line) or MDCK
783 *AF-6*$^{-/-}$ (gray dashed line) cells. Unpolarized monolayers of MDCK cell lines were infected with

784 10403S at MOI of 150:1. Gentamicin was added at 50 μg/ml to kill extracellular bacteria and
785 maintained in media thereafter. Each growth curve represents the means and standard deviations
786 of colony forming units (CFU) over time from three separate experiments performed in
787 triplicates. (B) Afadin limits initial *L. monocytogenes* invasion. Flow cytometry quantifying the
788 number of *L. monocytogenes*-containing MDCK and MDCK *AF-6*$^{-/-}$ cells 5 hours post infection.
789 Data were normalized to 1 for wild-type MDCK cells infected with Δ*actA L. monocytogenes* for
790 each experiment, and pooled from two independent experiments (each experiment is depicted by
791 different symbols). (C) Amount of transcytosis by wild-type (blue), Δ*inlP* (red), and Δ*actA*
792 (green) *L. monocytogenes* through MDCK and MDCK *AF-6*$^{-/-}$ monolayers. Data were normalized
793 to 1 for MDCK cells infected with wild-type *L. monocytogenes* for each experiment, and pooled
794 from four independent experiments (MDCK cells) or three independent experiments (MDCK
795 *AF-6*$^{-/-}$ cells). Each experiment is depicted by different symbols. (D) Amount of transcytosis by
796 wild-type, Δ*inlP*, and ΔLRR5 *L. monocytogenes* through MDCK monolayers. Data were
797 normalized to 1 for MDCK cells infected with wild-type *L. monocytogenes* for each experiment,
798 and pooled from three independent experiments. Each experiment is depicted by different
799 symbols.
800

801 **SUPPORTING INFORMATION CAPTIONS**

802 **Figure S1. Coomassie and silver stains showing fractions for mass spectrometry analysis.**
803 GST protein alone and InlP -GST fusion protein bound to glutathione-Sepharose resin were used
804 as bait for pull-down experiments with (+) or without (-) protein extracts from human placenta.
805 Shown on the left is Coomassie blue staining of each fraction, with the most abundant band in
806 each lane representing the bait protein. Shown on the right is silver staining of each fraction, with

807 the most abundant band in each lane representing the bait protein. The red boxes labeled A and B
808 show the two fractions extracted from gel and analyzed by mass spectrometry (see Sheet 1 and 2
809 in Supplementary Table 2).
810
811 **Figure S2. Structural and biochemical details on InlP Ca^{2+} interaction.** (A) Schematic view of
812 the interaction between the Ca^{2+} with the 3rd LRR loop of InlP. The amino acids D132 and E182,
813 which are involved in the interaction, are shown as sticks, water molecules as red spheres, and
814 hydrogen bonds as dashed lines. (B) Isothermal titration calorimetry results show Ca^{2+} binding to
815 InlP. The isotherm was fit by a one site binding model (N = 1.8 ± 0.1 site, K = 2.6E4 ± 6.5E3 M^{-1},
816 ΔH = -1176 ± 90.2 cal/mol, ΔS = 16.3 cal/mol/deg).
817
818 **Figure S3. Loading control by Coomassie staining and western blot analysis of pull down**
819 **experiments on InlPΔLRR8 mutant.** InlP-afadin binding pull-down experiments with ΔLRR8
820 mutant. GST protein alone (-), InlPΔLRR8-GST fusion protein (ΔLRR8), or InlP-GST (InlP)
821 bound to glutathione-sepharose resin were used as bait for pull-down experiments with protein
822 extracts from MDCK cell line. (A) Coomassie blue staining of each fraction, with the most
823 abundant band in each lane representing the bait protein. (B) Data shown are a western blot
824 analysis using anti-afadin antibodies. Actin was used as loading control.
825
826 **SUPPLEMENTARY TABLES**
827 **Supplementary Table 1. Yeast two-hybrid screening of human placenta library.**
828 **Supplementary Table 2. Mass spectrometry data from pull-down of InlP-GST interacting**
829 **with binding partners from human placental tissue.**

830 **Supplementary Table 3. Crystallographic Table.**

831 **Supplementary Table 4. Mass spectrometry data using InlP-GST, InlPΔLRR5-GST, or**

832 **Lmo2027-GST as baits to identify host binding partners in extracts from MDCK cell**

833 **cultures.**

834

835

836

837 **REFERENCES**

838 1. Faralla C, Rizzuto GA, Lowe DE, Kim B, Cooke C, Shiow LR, et al. InlP, a New
839 Virulence Factor with Strong Placental Tropism. Infect Immun. 2016;84(12):3584-96.
840 2. Janakiraman V. Listeriosis in Pregnancy: Diagnosis, Treatment, and Prevention. Reviews
841 in Obstetrics and Gynecology. 2008;1(4):179-85.
842 3. Robbins JR, Bakardjiev AI. Pathogens and the placental fortress. Curr Opin Microbiol.
843 2012;15(1):36-43.
844 4. Vázquez-Boland JA, Krypotou E, Scortti M. Listeria Placental Infection. mBio.
845 2017;8(3):e00949-17.
846 5. Vazquez-Boland JA, Kuhn M, Berche P, Chakraborty T, Dominguez-Bernal G, Goebel W,
847 et al. Listeria pathogenesis and molecular virulence determinants. Clin Microbiol Rev.
848 2001;14(3):584-640.
849 6. Mengaud J, Ohayon H, Gounon P, Mege RM, Cossart P. E-cadherin is the receptor for
850 internalin, a surface protein required for entry of L. monocytogenes into epithelial cells. Cell.
851 1996;84(6):923-32.
852 7. Lecuit M, Dramsi S, Gottardi C, Fedor-Chaiken M, Gumbiner B, Cossart P. A single
853 amino acid in E-cadherin responsible for host specificity towards the human pathogen Listeria
854 monocytogenes. Embo j. 1999;18(14):3956-63.
855 8. Pentecost M, Otto G, Theriot JA, Amieva MR. Listeria monocytogenes Invades the
856 Epithelial Junctions at Sites of Cell Extrusion. PLOS Pathogens. 2006;2(1):e3.
857 9. Tilney LG, Portnoy DA. Actin filaments and the growth, movement, and spread of the
858 intracellular bacterial parasite, Listeria monocytogenes. The Journal of Cell Biology.
859 1989;109(4):1597-608.
860 10. Robbins JR, Barth AI, Marquis H, de Hostos EL, Nelson WJ, Theriot JA. Listeria
861 monocytogenes exploits normal host cell processes to spread from cell to cell. J Cell Biol.
862 1999;146(6):1333-50.
863 11. Drevets DA, Jelinek TA, Freitag NE. Listeria monocytogenes-infected phagocytes can
864 initiate central nervous system infection in mice. Infect Immun. 2001;69(3):1344-50.
865 12. Bakardjiev AI, Theriot JA, Portnoy DA. Listeria monocytogenes traffics from maternal
866 organs to the placenta and back. PLoS Pathog. 2006;2(6):e66.
867 13. Portnoy DA, Auerbuch V, Glomski IJ. The cell biology of Listeria monocytogenes
868 infection: the intersection of bacterial pathogenesis and cell-mediated immunity. The Journal of
869 Cell Biology. 2002;158(3):409-14.
870 14. Le Monnier A, Autret N, Join-Lambert OF, Jaubert F, Charbit A, Berche P, et al. ActA is
871 required for crossing of the fetoplacental barrier by Listeria monocytogenes. Infect Immun.
872 2007;75(2):950-7.
873 15. Bakardjiev AI, Stacy BA, Portnoy DA. Growth of Listeria monocytogenes in the guinea
874 pig placenta and role of cell-to-cell spread in fetal infection. J Infect Dis. 2005;191(11):1889-97.
875 16. Drevets DA. Dissemination of Listeria monocytogenes by infected phagocytes. Infect
876 Immun. 1999;67(7):3512-7.
877 17. Tilburgs T, Crespo AC, van der Zwan A, Rybalov B, Raj T, Stranger B, et al. Human
878 HLA-G+ extravillous trophoblasts: Immune-activating cells that interact with decidual leukocytes.
879 Proc Natl Acad Sci U S A. 2015;112(23):7219-24.
880 18. Guleria I, Pollard JW. The trophoblast is a component of the innate immune system during
881 pregnancy. Nat Med. 2000;6(5):589-93.

882 19. Zeldovich VB, Bakardjiev AI. Host Defense and Tolerance: Unique Challenges in the
883 Placenta. PLOS Pathogens. 2012;8(8):e1002804.
884 20. Robbins JR, Skrzypczynska KM, Zeldovich VB, Kapidzic M, Bakardjiev AI. Placental
885 syncytiotrophoblast constitutes a major barrier to vertical transmission of Listeria monocytogenes.
886 PLoS Pathog. 2010;6(1):e1000732.
887 21. Zeldovich VB, Clausen CH, Bradford E, Fletcher DA, Maltepe E, Robbins JR, et al.
888 Placental Syncytium Forms a Biophysical Barrier against Pathogen Invasion. PLoS Pathog.
889 2013;9(12):e1003821.
890 22. Kobe B, Kajava AV. The leucine-rich repeat as a protein recognition motif. Current
891 Opinion in Structural Biology. 2001;11(6):725-32.
892 23. Shen Y, Naujokas M, Park M, Ireton K. InlB-Dependent Internalization of Listeria Is
893 Mediated by the Met Receptor Tyrosine Kinase. Cell. 2000;103(3):501-10.
894 24. Bierne H, Sabet C, Personnic N, Cossart P. Internalins: a complex family of leucine-rich
895 repeat-containing proteins in Listeria monocytogenes. Microbes Infect. 2007;9(10):1156-66.
896 25. Anderson WF. Structural Genomics and Drug Discovery for Infectious Diseases.
897 Infectious disorders drug targets. 2009;9(5):507-17.
898 26. Kim Y, Bigelow L, Borovilos M, Dementieva I, Duggan E, Eschenfeldt W, et al. Chapter
899 3. High-throughput protein purification for x-ray crystallography and NMR. Adv Protein Chem
900 Struct Biol. 2008;75:85-105.
901 27. Otwinowski Z, Minor W. Processing of X-ray diffraction data collected in oscillation
902 mode. Methods Enzymol. 1997;276:307-26.
903 28. Murshudov GN, Skubak P, Lebedev AA, Pannu NS, Steiner RA, Nicholls RA, et al.
904 REFMAC5 for the refinement of macromolecular crystal structures. Acta crystallographica
905 Section D, Biological crystallography. 2011;67(Pt 4):355-67.
906 29. Emsley P, Cowtan K. Coot: model-building tools for molecular graphics. Acta Crystallogr
907 D Biol Crystallogr. 2004;60(Pt 12 Pt 1):2126-32.
908 30. Rizzuto GA, Kapidzic M, Gormley M, Bakardjiev AI. Human Placental and Decidual
909 Organ Cultures to Study Infections at the Maternal-fetal Interface. J Vis Exp. 2016(113).
910 31. Bakardjiev AI, Stacy BA, Fisher SJ, Portnoy DA. Listeriosis in the pregnant guinea pig: a
911 model of vertical transmission. Infect Immun. 2004;72(1):489-97.
912 32. Bastounis E, Meili R, Álvarez-González B, Francois J, del Álamo JC, Firtel RA, et al.
913 Both contractile axial and lateral traction force dynamics drive amoeboid cell motility. The
914 Journal of Cell Biology. 2014;204(6):1045-61.
915 33. Lamason RL, Bastounis E, Kafai NM, Serrano R, Del Alamo JC, Theriot JA, et al.
916 Rickettsia Sca4 Reduces Vinculin-Mediated Intercellular Tension to Promote Spread. Cell.
917 2016;167(3):670-83.e10.
918 34. Gui L, Wereley ST. A correlation-based continuous window-shift technique to reduce the
919 peak-locking effect in digital PIV image evaluation. Exp Fluids. 2002;32:506-17.
920 35. del Álamo JC, Meili R, Alonso-Latorre B, Rodríguez-Rodríguez J, Aliseda A, Firtel RA,
921 et al. Spatio-temporal analysis of eukaryotic cell motility by improved force cytometry. Proc Nat
922 Acad Sci. 2007;104(33):13343-8.
923 36. Banerjee I, Carrion K, Serrano R, Dyo J, Sasik R, Lund S, et al. Cyclic stretch of
924 embryonic cardiomyocytes increases proliferation, growth, and expression while repressing Tgf-β
925 signaling. Journal of Molecular and Cellular Cardiology. 2015;79:133-44.

926 37. Zeldovich VB, Robbins JR, Kapidzic M, Lauer P, Bakardjiev AI. Invasive extravillous
927 trophoblasts restrict intracellular growth and spread of Listeria monocytogenes. PLoS Pathog.
928 2011;7(3):e1002005.
929 38. Ortega FE, Rengarajan M, Chavez N, Radhakrishnan P, Gloerich M, Bianchini J, et al.
930 Adhesion to the host cell surface is sufficient to mediate Listeria monocytogenes entry into
931 epithelial cells. Mol Biol Cell. 2017.
932 39. Zhou X, Massol RH, Nakamura F, Chen X, Gewurz BE, Davis BM, et al. Remodeling of
933 the Intestinal Brush Border Underlies Adhesion and Virulence of an Enteric Pathogen. mBio.
934 2014;5(4):e01639-14.
935 40. Mandai K, Rikitake Y, Shimono Y, Takai Y. Afadin/AF-6 and canoe: roles in cell
936 adhesion and beyond. Prog Mol Biol Transl Sci. 2013;116:433-54.
937 41. Ikeda W, Nakanishi H, Miyoshi J, Mandai K, Ishizaki H, Tanaka M, et al. Afadin: A key
938 molecule essential for structural organization of cell-cell junctions of polarized epithelia during
939 embryogenesis. J Cell Biol. 1999;146(5):1117-32.
940 42. Zhadanov AB, Provance DW, Jr., Speer CA, Coffin JD, Goss D, Blixt JA, et al. Absence
941 of the tight junctional protein AF-6 disrupts epithelial cell-cell junctions and cell polarity during
942 mouse development. Curr Biol. 1999;9(16):880-8.
943 43. Sawyer JK, Harris NJ, Slep KC, Gaul U, Peifer M. The Drosophila afadin homologue
944 Canoe regulates linkage of the actin cytoskeleton to adherens junctions during apical constriction.
945 The Journal of Cell Biology. 2009;186(1):57-73.
946 44. Schubert WD, Urbanke C, Ziehm T, Beier V, Machner MP, Domann E, et al. Structure of
947 internalin, a major invasion protein of Listeria monocytogenes, in complex with its human
948 receptor E-cadherin. Cell. 2002;111(6):825-36.
949 45. Serra-Picamal X, Conte V, Vincent R, Anon E, Tambe DT, Bazellieres E, et al.
950 Mechanical waves during tissue expansion. Nature Physics. 2012;8:628.
951 46. Bazellières E, Conte V, Elosegui-Artola A, Serra-Picamal X, Bintanel-Morcillo M, Roca-
952 Cusachs P, et al. Control of cell–cell forces and collective cell dynamics by the intercellular
953 adhesome. Nat Cell Biol. 2015;17(4):409-20.
954 47. Rengarajan M, Hayer A, Theriot JA. Endothelial Cells Use a Formin-Dependent
955 Phagocytosis-Like Process to Internalize the Bacterium Listeria monocytogenes. PLoS Pathog.
956 2016;12(5):e1005603.
957 48. Ferrell N, Groszek J, Li L, Smith R, Butler RS, Zorman CA, et al. Basal lamina secreted
958 by MDCK cells has size- and charge-selective properties. Am J Physiol Renal Physiol.
959 2011;300(1):F86-90.
960 49. PrabhuDas M, Bonney E, Caron K, Dey S, Erlebacher A, Fazleabas A, et al. Immune
961 mechanisms at the maternal-fetal interface: perspectives and challenges. Nat Immunol. 16. United
962 States2015. p. 328-34.
963 50. Parida SK, Domann E, Rohde M, Muller S, Darji A, Hain T, et al. Internalin B is essential
964 for adhesion and mediates the invasion of Listeria monocytogenes into human endothelial cells.
965 Mol Microbiol. 1998;28(1):81-93.
966 51. Kirchner M, Higgins DE. Inhibition of ROCK activity allows InlF-mediated invasion and
967 increased virulence of Listeria monocytogenes. Mol Microbiol. 2008;68(3):749-67.
968 52. Sabet C, Lecuit M, Cabanes D, Cossart P, Bierne H. LPXTG protein InlJ, a newly
969 identified internalin involved in Listeria monocytogenes virulence. Infect Immun.
970 2005;73(10):6912-22.

971 53. Tsurumi H, Kurihara H, Miura K, Tanego A, Ohta Y, Igarashi T, et al. Afadin is localized
972 at cell–cell contact sites in mesangial cells and regulates migratory polarity. Laboratory
973 Investigation. 2015;96:49.
974 54. Gouin E, Adib-Conquy M, Balestrino D, Nahori M-A, Villiers V, Colland F, et al. The
975 Listeria monocytogenes InlC protein interferes with innate immune responses by targeting the IκB
976 kinase subunit IKKα. Proceedings of the National Academy of Sciences of the United States of
977 America. 2010;107(40):17333-8.
978 55. Rajabian T, Gavicherla B, Heisig M, Muller-Altrock S, Goebel W, Gray-Owen SD, et al.
979 The bacterial virulence factor InlC perturbs apical cell junctions and promotes cell-to-cell spread
980 of Listeria. Nat Cell Biol. 2009;11(10):1212-8.
981 56. Christensen KA, Myers JT, Swanson JA. pH-dependent regulation of lysosomal calcium
982 in macrophages. J Cell Sci. 2002;115(Pt 3):599-607.
983 57. Shaughnessy LM, Hoppe AD, Christensen KA, Swanson JA. Membrane perforations
984 inhibit lysosome fusion by altering pH and calcium in Listeria monocytogenes vacuoles. Cell
985 Microbiol. 2006;8(5):781-92.
986 58. Thai TL, Yu L, Galarza-Paez L, Wu MM, Lam HY, Bao HF, et al. The Polarized Effect of
987 Intracellular Calcium on the Renal Epithelial Sodium Channel Occurs as a Result of Subcellular
988 Calcium Signaling Domains Maintained by Mitochondria. J Biol Chem. 2015;290(48):28805-11.
989 59. Kiselyov K, Wang X, Shin DM, Zang W, Muallem S. Calcium signaling complexes in
990 microdomains of polarized secretory cells. Cell Calcium. 2006;40(5-6):451-9.
991 60. Cantero Mdel R, Cantiello HF. Calcium transport and local pool regulate polycystin-2
992 (TRPP2) function in human syncytiotrophoblast. Biophys J. 2013;105(2):365-75.
993 61. Saenz HL, Engel P, Stoeckli MC, Lanz C, Raddatz G, Vayssier-Taussat M, et al. Genomic
994 analysis of Bartonella identifies type IV secretion systems as host adaptability factors. Nat Genet.
995 2007;39(12):1469-76.
996 62. Roux CM, Rolan HG, Santos RL, Beremand PD, Thomas TL, Adams LG, et al. Brucella
997 requires a functional Type IV secretion system to elicit innate immune responses in mice. Cell
998 Microbiol. 2007;9(7):1851-69.
999 63. Coburn B, Sekirov I, Finlay BB. Type III secretion systems and disease. Clin Microbiol
1000 Rev. 2007;20(4):535-49.
1001 64. Backert S, Meyer TF. Type IV secretion systems and their effectors in bacterial
1002 pathogenesis. Curr Opin Microbiol. 2006;9(2):207-17.
1003 65. Tanaka-Okamoto M, Hori K, Ishizaki H, Itoh Y, Onishi S, Yonemura S, et al. Involvement
1004 of afadin in barrier function and homeostasis of mouse intestinal epithelia. J Cell Sci. 2011;124(Pt
1005 13):2231-40.
1006 66. Severson EA, Lee WY, Capaldo CT, Nusrat A, Parkos CA. Junctional adhesion molecule
1007 A interacts with Afadin and PDZ-GEF2 to activate Rap1A, regulate beta1 integrin levels, and
1008 enhance cell migration. Mol Biol Cell. 2009;20(7):1916-25.
1009 67. Yamamoto T, Mori T, Sawada M, Matsushima H, Ito F, Akiyama M, et al. Loss of AF-
1010 6/afadin induces cell invasion, suppresses the formation of glandular structures and might be a
1011 predictive marker of resistance to chemotherapy in endometrial cancer. BMC Cancer.
1012 2015;15:275.
1013 68. Iwasawa N, Negishi M, Oinuma I. R-Ras controls axon branching through afadin in
1014 cortical neurons. Molecular Biology of the Cell. 2012;23(14):2793-804.

1015 69. Robbins JR, Zeldovich VB, Poukchanski A, Boothroyd JC, Bakardjiev AI. Tissue barriers
1016 of the human placenta to infection with Toxoplasma gondii. Infect Immun. 2012;80(1):418-28.
1017 70. Groschwitz KR, Hogan SP. Intestinal barrier function: molecular regulation and disease
1018 pathogenesis. J Allergy Clin Immunol. 2009;124(1):3-20; quiz 1-2.
1019 71. Melton-Witt JA, Rafelski SM, Portnoy DA, Bakardjiev AI. Oral Infection with Signature-
1020 Tagged Listeria monocytogenes Reveals Organ-Specific Growth and Dissemination Routes in
1021 Guinea Pigs. Infection and Immunity. 2012;80(2):720-32.

1022

Figure 1

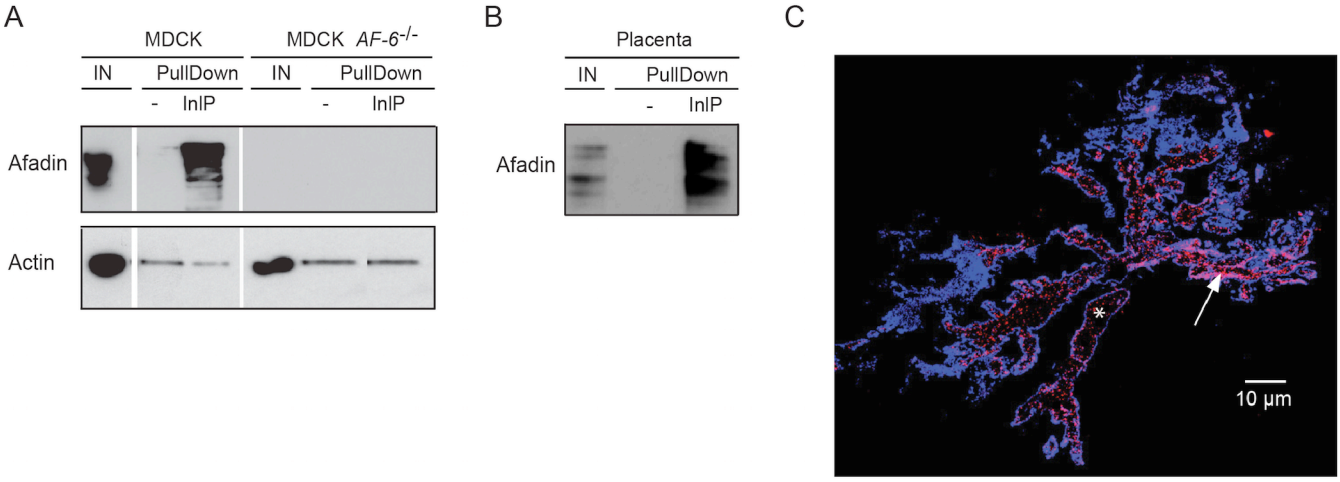
A
MDCK
MDCK AF-6-/-
IN
PullDown
IN
PullDown
-
InIP
-
InIP
Afadin
Actin
B
Placenta
IN
PullDown
-
InIP
Afadin
C
10 µm

Figure 2

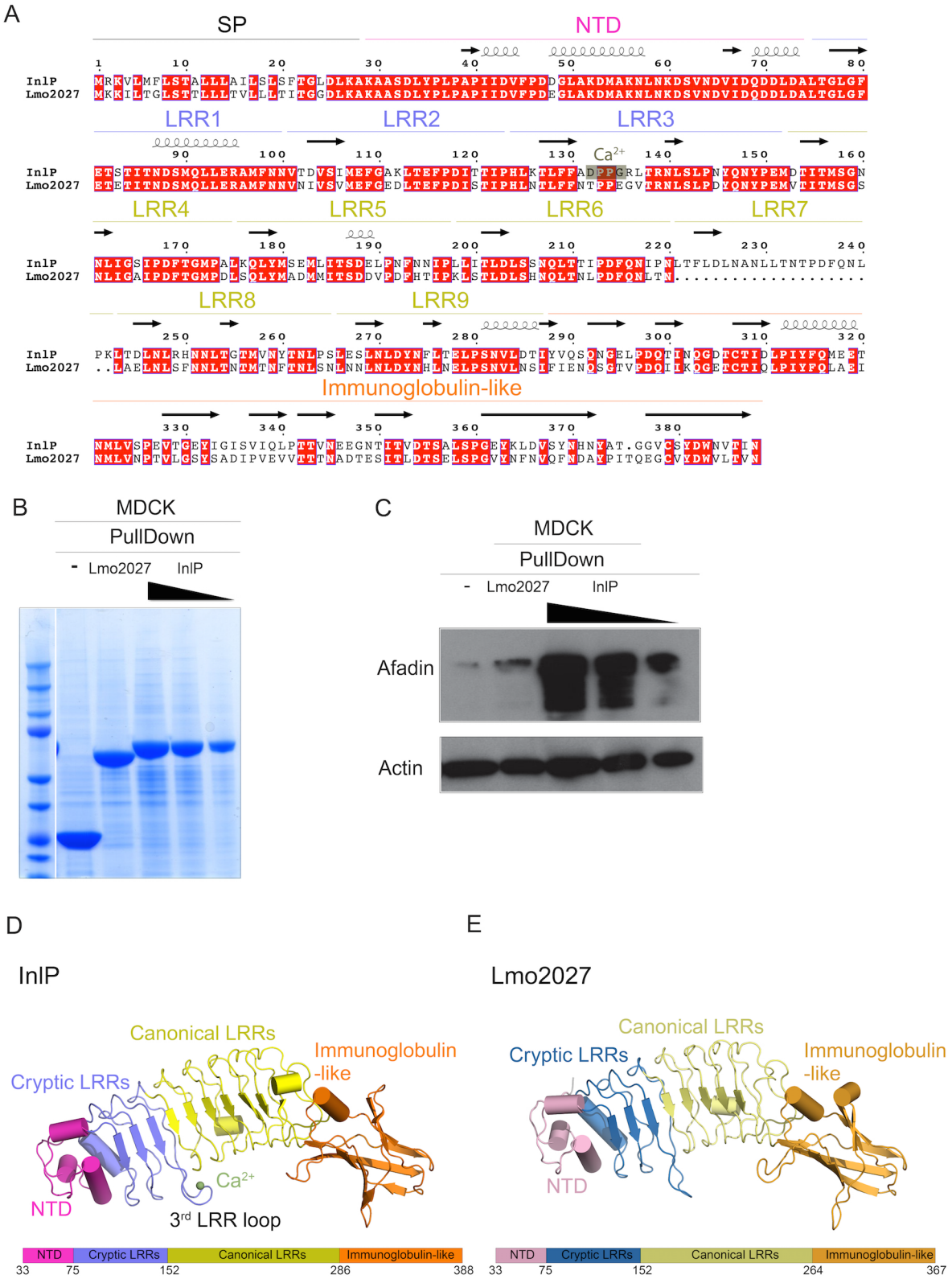
A
SP
NTD
InlP
Lmo2027
LRR1
LRR2
LRR3
Ca2+
LRR4
LRR5
LRR6
LRR7
LRR8
LRR9
Immunoglobulin-like
B
MDCK
PullDown
- Lmo2027 InlP
C
MDCK
PullDown
- Lmo2027 InlP
Afadin
Actin
D
InlP
Canonical LRRs
Cryptic LRRs
Immunoglobulin -like
NTD
Ca2+
3rd LRR loop
NTD Cryptic LRRs Canonical LRRs Immunoglobulin-like
33 75 152 286 388
E
Lmo2027
Canonical LRRs
Cryptic LRRs
Immunoglobulin -like
NTD
NTD Cryptic LRRs Canonical LRRs Immunoglobulin-like
33 75 152 264 367

Figure 3

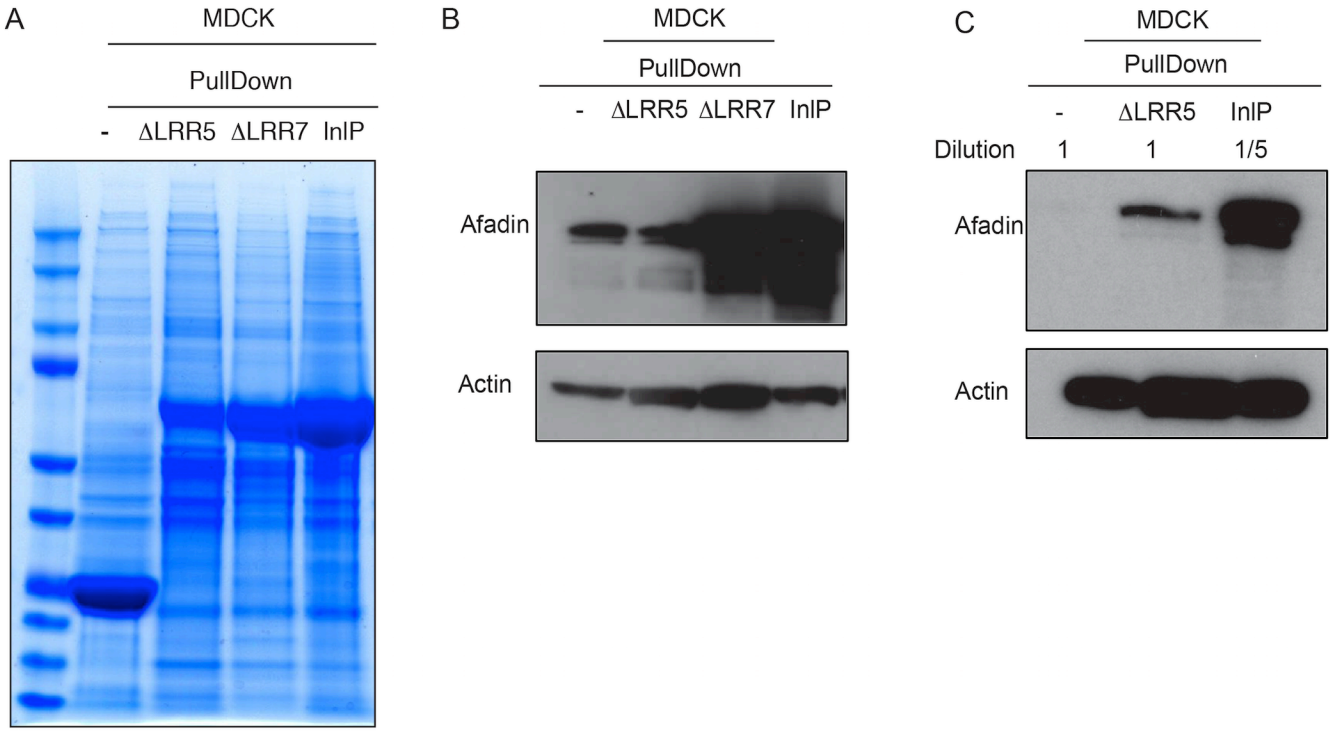
A
MDCK
PullDown
-
ΔLRR5
ΔLRR7
InlP
B
MDCK
PullDown
-
ΔLRR5
ΔLRR7
InlP
Afadin
Actin
C
MDCK
PullDown
-
ΔLRR5
InlP
Dilution
1
1
1/5
Afadin
Actin

Figure 4

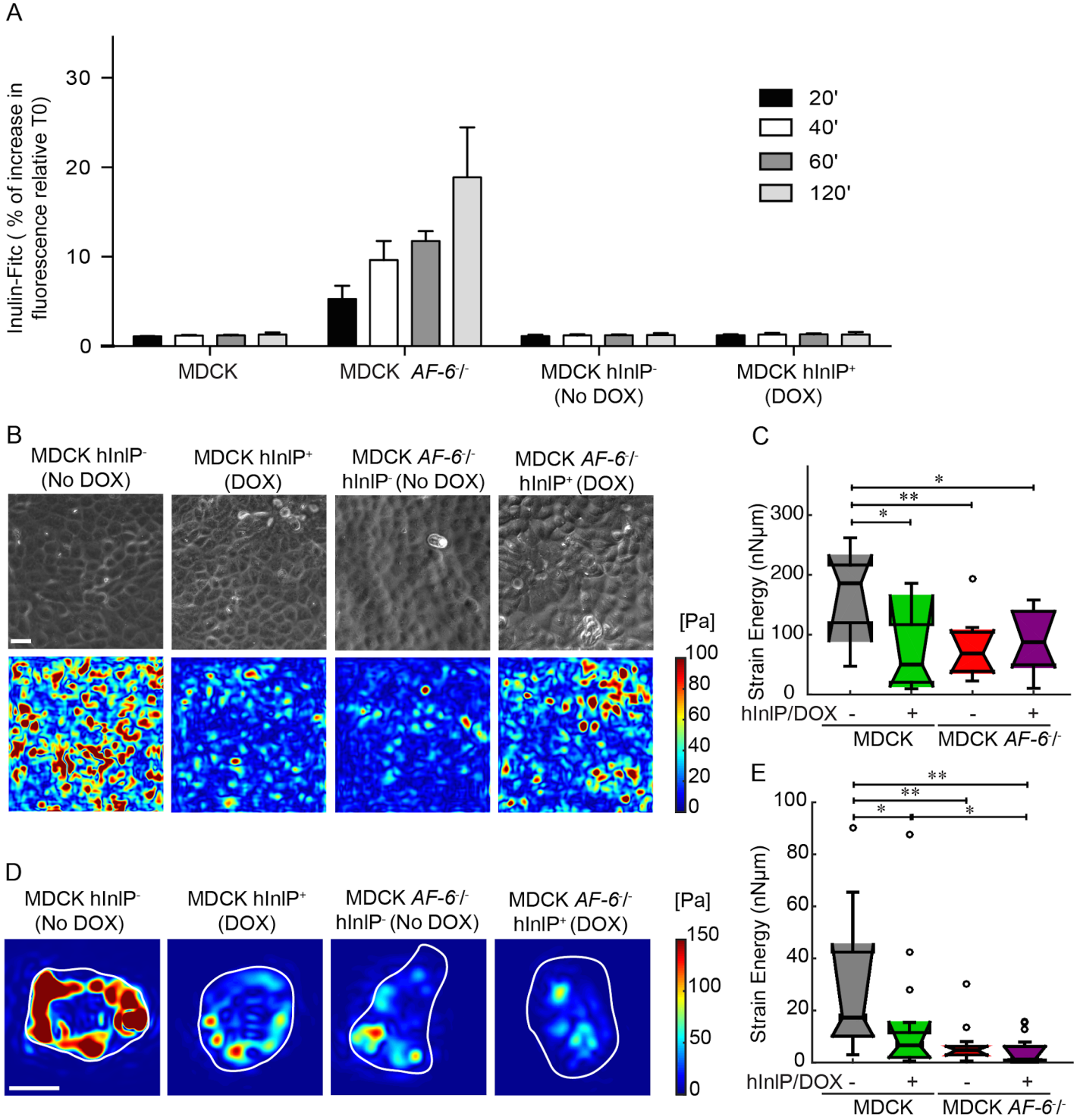
A
Inulin-Fitc (% of increase in fluorescence relative T0)
30
20
10
0
20'
40'
60'
120'
MDCK
MDCK AF-6-/-
MDCK hInIP-
(No DOX)
MDCK hInIP+
(DOX)
B
MDCK hInIP-
(No DOX)
MDCK hInIP+
(DOX)
MDCK AF-6-/-
hInIP- (No DOX)
MDCK AF-6-/-
hInIP+ (DOX)
[Pa]
100
80
60
40
20
0
C
Strain Energy (nNµm)
300
200
100
0
*
**
*
hInIP/DOX - + - +
MDCK
MDCK AF-6-/-
D
MDCK hInIP-
(No DOX)
MDCK hInIP+
(DOX)
MDCK AF-6-/-
hInIP- (No DOX)
MDCK AF-6-/-
hInIP+ (DOX)
[Pa]
150
100
50
0
E
Strain Energy (nNµm)
100
80
60
40
20
0
**
**
*
*
hInIP/DOX - + - +
MDCK
MDCK AF-6-/-

Figure 5

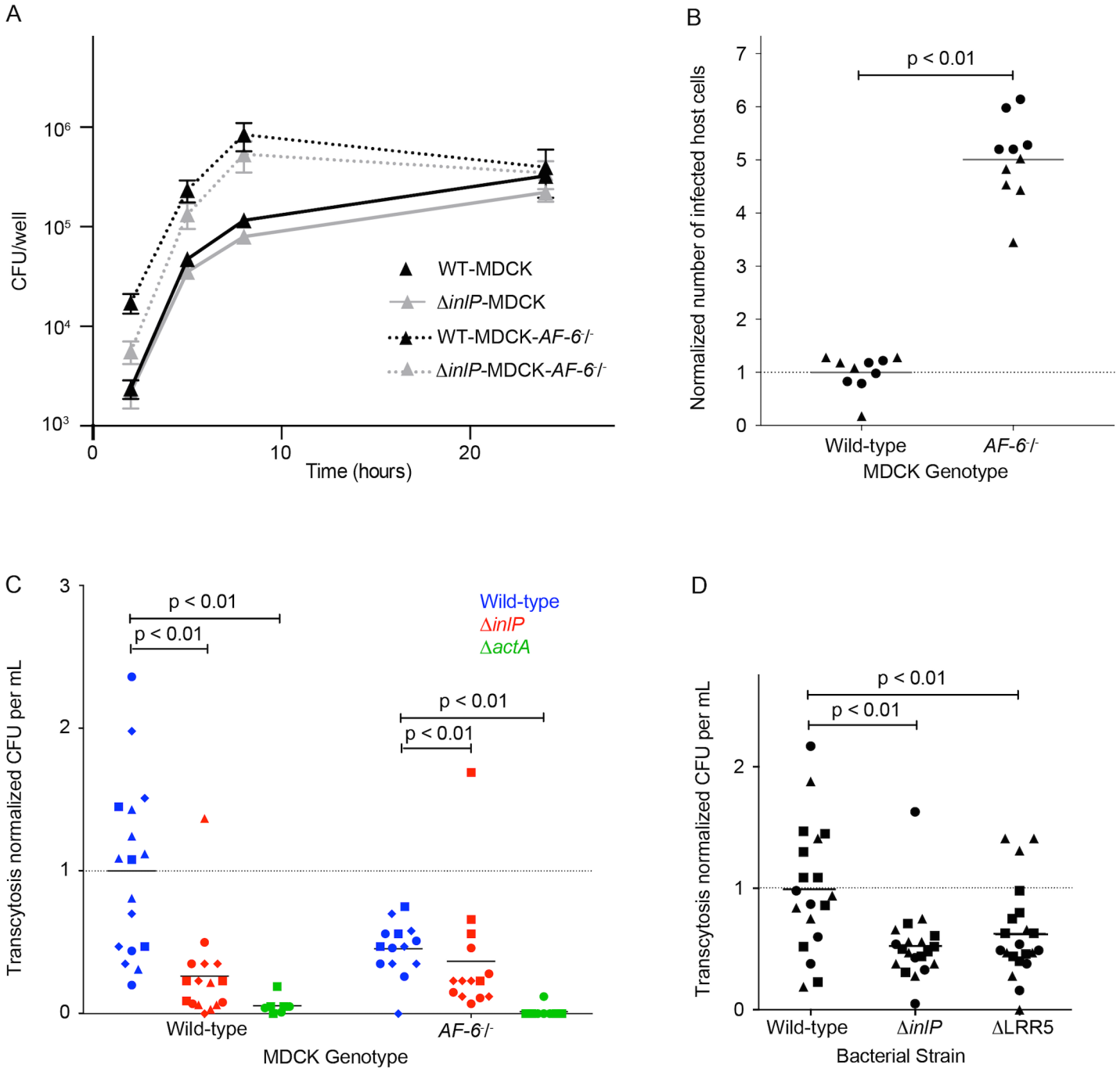
A
CFU/well
10^6
10^5
10^4
10^3
0
10
20
Time (hours)
WT-MDCK
ΔinlP-MDCK
WT-MDCK-AF-6-/-
ΔinlP-MDCK-AF-6-/-
B
Normalized number of infected host cells
p < 0.01
Wild-type
AF-6-/-
MDCK Genotype
C
Transcytosis normalized CFU per mL
p < 0.01
p < 0.01
p < 0.01
p < 0.01
Wild-type
ΔinlP
ΔactA
Wild-type
AF-6-/-
MDCK Genotype
D
Transcytosis normalized CFU per mL
p < 0.01
p < 0.01
Wild-type
ΔinlP
ΔLRR5
Bacterial Strain

Suppl. Figure 1

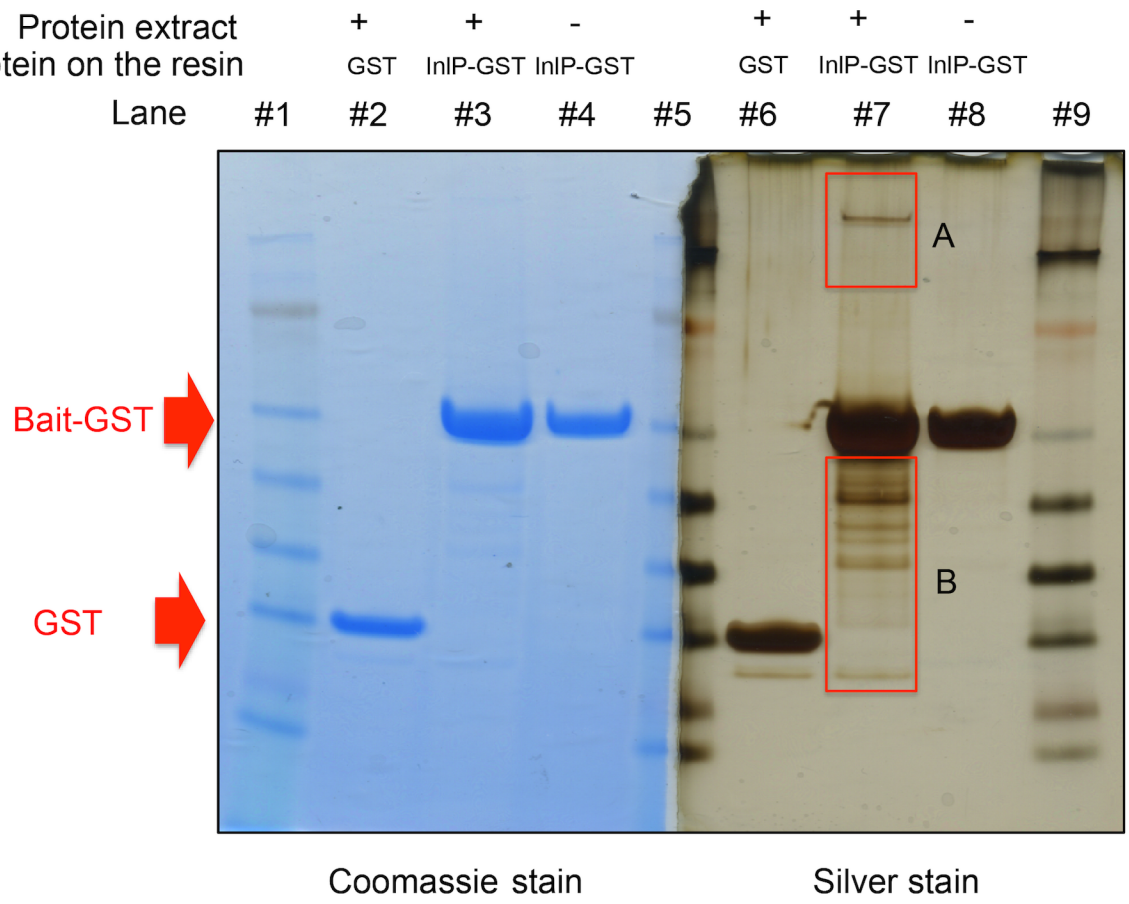

Suppl. Figure 2

A

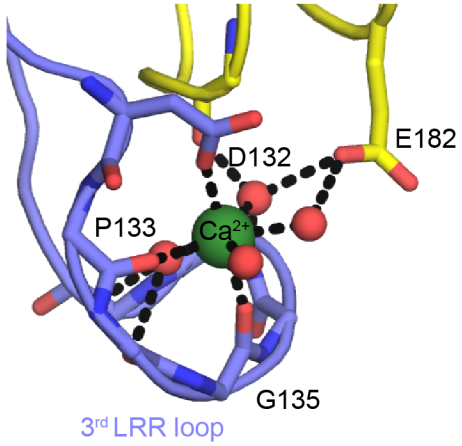

B

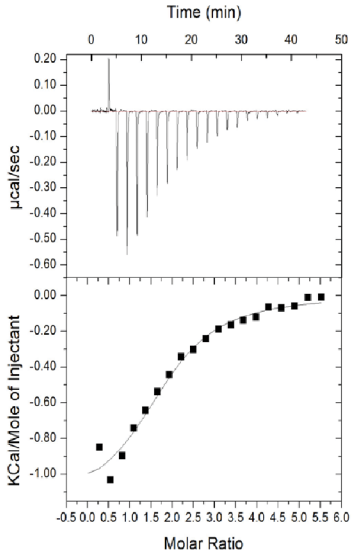

Suppl. Figure 3

A

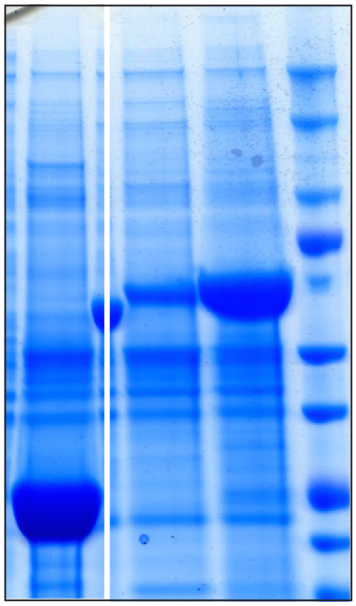

B

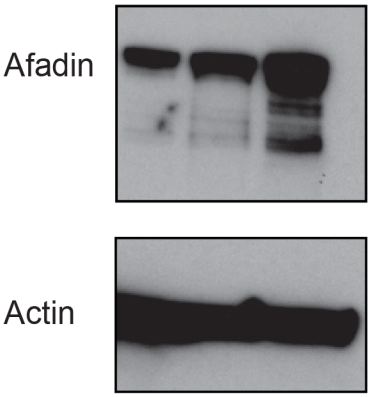

Table 1. Yeast two-hybrid screening of human placenta library
Results summary listing the protein partners identified (gene name), the number of independent clones and the global PBS [a]. Ordering is performed based on global PBS and then on number of clones. Afadin is indicated in red.

Gene name	Number of independent clones	Global PBS [a]
RPS8	26	A
RBM5	14	A
TSHZ1	12	A
RPL5	9	A
AEBP1	7	A
NAB2	6	A
THAP3	6	A
NAB1	4	A
DNMT3A	5	B
SAFB	5	B
ZNF653	5	B
EXOSC3	4	B
RPL7A	4	B
AF6	3	B
FLJ22329	3	B
SP3	3	B
ZNF653	5	B
ZNF6	3	C
CDC27	2	C
EPS8L2	2	C
PHF23	2	C
ZNF283	2	C

[a]Global Predicted Biological Score (PBS). Confidence score of each interaction. A: very high confidence interaction; B: high confidence in the interaction; and C: good confidence in the interaction.

Table 2. Mass spectrometry data from pull-down of InlP-GST interacting with binding partners from human placental tissue.

Proteins identified with more than 10 unique peptides are outlined below. Black and blue correspond to sections A and B respectively (see Supplementary Figure 1). Afadin is indicated in red.

Gene name	Unique peptides	Total peptides
FLNA	79	124
AHNAK	54	67
DYNC1H1	39	54
TPR	29	39
FLNB	29	38
IQGAP1	25	31
COL6A3	24	27
CLTC	20	26
AF6	18	23
TNKS1BP1	15	19
MYH9	14	17
KIF5B	13	15
FN1	11	14
COL14A1	11	12
ANXA2	18	38
VIM	16	27
CALD1	13	27
ANXA1	12	23
ACADVL	12	16
GSTP1	11	24
ANXA5	11	14

Table 3. Crystallographic Table

Data Collection and Refinement Statistics[a]

	InlP	Lmo2027
PDB code	5HL3	5KZS
Data Collection		
Resolution range, Å	30.00-1.40 (1.42-1.40)	30.00-2.30 (2.34-2.30)
Space group	$P4_12_12$	I_4
Unit cell dimensions		
a,b,c, Å	a & b= 72.9 c = 179.5	a & b = 157.8 c = 36.3
α, β, γ, degrees	α, β, γ = 90	α, β, γ = 90
Completeness, %	99.8 (100)	98.6 (99.6)
No. reflections	180423 (9031)	20005 (1429)
Redundancy	45.6 (5.3)	6.2 (4.5)
$\langle I/\sigma(I) \rangle$	30.2 (2.6)	79.7 (2.0)
R_{merge}, %	7.9 (65.3)	9.0 (57.1)
Refinement statistics		
R-factor (R_{work}/R_{free})[b]	16.0/17.6	22.8/27.9
No. atoms		
Protein	2935	2377
Waters	828	26
Ca^{2+}	8	n/a
R.M.S. deviations		
Bond lengths, Å	0.011	0.009
Bond angles, degrees	1.51	1.47
Ramachandran analysis		
Favored regions, %	96	95
Allowed regions, %	100	99
Disallowed regions, %	0	1

[a] Highest resolution shell in parenthesis.

[b] Definition of R_{work}, R_{free}: $R=\Sigma_{hkl}\big||F_{obs}|-|F_{calc}|\big| / \Sigma_{hkl}|F_{obs}|$, where *hkl* are the reflection indices used in refinement for **R_{work}, and 5% not used in refinement for R_{free}**. F_{obs} and F_{calc} are structure factors deduced from measured intensities or calculated from the model, respectively.

Table 4. Mass spectrometry data using InlP-GST, InlPΔLRR5-GST, or Lmo2027-GST as baits to identify host binding partners in extracts from MDCK cell cultures.

Listed are the names of the genes of proteins identified as enriched for by full-length InlP with an arbitrary cutoff of 10 unique peptides. Binding to InlP was categorized as specific if there was at least a 2-fold difference in the number of unique peptides. Afadin is indicated in red.

Gene symbol	MWT (kDa)	InlP-GST	ΔLRR5-GST	Lmo2027-GST
Category 1: Proteins enriched by InlP but not ΔLRR5 or Lmo2027				
MLLT4/AF-6	206.68	20	1	4
IDH3B	42.16	15	5	2
ARPC2	34.31	10	0	4
PCYT1A	41.7	10	3	2
Category 2: Proteins enriched by InlP and ΔLRR5 but not Lmo2027				
GCN1L1	292.57	43	58	9
ARAP3	169.74	21	24	4
UTRN	394.22	14	27	3
TRIM33	122.46	11	15	1
TANC2	219.51	10	16	0
PC	129.55	10	9	4
MSH2	104.68	10	11	0
POLDIP2	42.01	10	8	3
CDK1	34.07	10	6	0
Category 3: Proteins enriched by all three baits				
MYO6	149.6	26	32	43
PHLDB1	151.07	19	11	12
POLR2B	133.81	17	14	8
OPLAH	137.37	16	16	10
SIPA1L1	199.9	13	15	10
MSH6	152.69	13	14	9
PKP3	87.03	13	13	8
DOCK7	242.41	12	7	21
TBC1D4	146.47	12	13	9